Correspondence to:
P. Narenpitak,
pornampai.nar@nectec.or.th

The Sugar-To-Flower Shallow Cumulus Transition Under the Influences of Diel Cycle and Free-Tropospheric Mineral Dust

Pornampai Narenpitak[1,2,3] , **Jan Kazil**[2,3] , **Takanobu Yamaguchi**[2,3] , **Patricia K. Quinn**[4] , and **Graham Feingold**[3]

[1]Data-Driven Simulation and Systems Research Team, National Electronics and Computer Technology Center, Khlong Luang, Thailand, [2]Cooperative Institute for Research in Environmental Sciences, University of Colorado Boulder, Boulder, CO, USA, [3]National Oceanic and Atmospheric Administration, Chemical Sciences Laboratory, Boulder, CO, USA, [4]National Oceanic and Atmospheric Administration, Pacific Marine Environmental Laboratory, Seattle, WA, USA

Abstract A shallow cumulus cloud transition from a sugar to flower type of organization occurred under a layer of mineral dust on 2 February 2020, during the multinational Atlantic Tradewind Ocean-Atmosphere Mesoscale Interaction Campaign (ATOMIC) and the Elucidating the Role of Clouds-Circulation Coupling in Climate (EUREC4A) campaigns. Lagrangian large eddy simulations following an airmass trajectory along the tradewinds are used to explore radiative impacts of the diel cycle and mineral dust on the sugar-to-flower (S2F) cloud transition. The large-scale meteorological forcing is derived from the European Center for Medium-Range Weather Forecasts Reanalysis Fifth Generation and based on aerosol measurements from the U.S. Ronald H. Brown Research Vessel and the French ATR-42 Research Aircraft during the field campaigns. A 12-hr delay in the diel cycle accelerates the S2F transition at night, leading to more cloud liquid water and precipitation. The aggregated clouds generate more and stronger cold pools, which alter the original mechanism responsible for the organization. Although there is still mesoscale moisture convergence in the cloud layer, the near-surface divergence associated with cold pools transports the subcloud moisture to the drier surrounding regions. New convection forms along the cold-pool edges, generating new flower clouds. The modulation of the surface radiative budget by free-tropospheric mineral dust poses a less dramatic effect on the S2F transition. Mineral dust releases longwave radiation, reducing the cloud amount at night, and absorbs shortwave radiation during the day, cooling the boundary-layer temperature and increasing the overall cloud amount. Cloud-top radiative heating because of more clouds strengthens the mesoscale organization, enlarging the aggregate areas, and increasing the cloud amount further.

Plain Language Summary During a joint field study called ATOMIC and EUREC4A, a transition between two cloud systems took place during the day on 2 February 2020. Very small and shallow clouds called "sugar" transitioned into deeper and wider cloud aggregates called "flowers." A dense mineral-dust layer was also observed above the tradewind cumulus cloud field, likely modulating the radiation interacting with the clouds. High-resolution simulations are applied to help understand the same cloud transition as if it had taken place at night, and to explore the impacts of mineral dust on the transition. A 12-hr delay in the daily cycle such that the transition occurs at night affects the cloud transition more significantly than when the transition occurs during the day under a layer of mineral dust. The cloud transition that occurs at night produces more clouds and rain. The mineral dust blocks the solar radiation and cools the air beneath during the day, but does not change the cloud and rain amount as much.

1. Introduction

Tradewind shallow cumulus clouds play an important role in Earth's radiation budget. These clouds are ubiquitous over tropical and subtropical oceans and reflect solar radiation, increasing the planetary albedo and cooling the boundary layer. The low-level clouds are a leading source of climate uncertainty in global climate models (e.g., Andrews et al., 2012; Bony & Dufresne, 2005; Boucher et al., 2013; Medeiros et al., 2008; Zelinka et al., 2016, 2020, and others). The uncertainty arises from challenges in representing the cloud liquid water, cloud structure, spatial patterns, precipitation and other internal processes that modulate the radiative properties of the clouds (Blossey et al., 2013; Bretherton et al., 2013; Nuijens & Siebesma, 2019; Rieck et al., 2012; Stevens et al., 2001; Xu et al., 2010; Zhang et al., 2013). In addition, shallow cumulus clouds are also sensitive to humidity and temperature of the boundary layer, which can be modulated not only by the global surface temperature

but also by radiation through other processes such as the diel cycle, precipitation, aerosol, and other atmospheric constituents.

Recent studies have classified the mesoscale organization of marine shallow cumuli using satellite images into four states: sugar, gravel, fish, and flowers (Bony et al., 2020; Rasp et al., 2020; Schulz et al., 2021; Stevens et al., 2020). Sugar clouds are small and shallow, and reflect the least amount of solar radiation among these four states. Gravel clouds exhibit arc-shaped forms. Fish occurs in an elongated structure with distinct cloudy and clear-sky portions. Flowers are circular and often appear in multiple aggregates surrounded by dry areas. Flowers usually have the highest cloud fraction among these four organization types.

Previous studies show that cloud organization and cloud amount are tightly connected with precipitation. To understand the precipitation formation of shallow cumuli, the Rain in Cumulus over the Ocean (RICO) project was deployed using surface observations, ship-based measurements and research aircrafts over the Atlantic Ocean in November 2004–January 2005 (Rauber et al., 2007). A higher amount of moisture in the boundary layer promotes deeper clouds that contain higher cloud liquid water, hence often rain more, reducing the cloud amount (Nuijens et al., 2009, 2017). Some studies suggest that the mesoscale organization of shallow cumuli can accelerate precipitation onset, further depleting the clouds (Bretherton & Blossey, 2017; vanZanten et al., 2011). Precipitation also leads to the formation of cold pools, which are mesoscale patterns of arc-shaped clouds surrounding the regions of colder air and precipitating downdrafts (Zuidema et al., 2012, 2017). Some studies suggest that cold pools themselves are a dominant mechanism that leads to mesoscale cloud organization (Seifert & Heus, 2013).

Boundary layer radiative heating or cooling also modulates the depth, brightness, organization, and other properties of the clouds. Sufficiently strong boundary-layer radiative cooling can lead to a cooler boundary layer that modulates the depth of the shallow circulation (Naumann et al., 2017). If the enhanced boundary-layer radiative cooling is balanced by stronger downward entrainment heat flux, the system could respond by increasing the updraft mass flux and thus the cloud fraction given that it does not precipitate (Narenpitak & Bretherton, 2019). Another factor that modulates the radiative heating or cooling rate is the diel cycle. Vial et al. (2019); Vial et al. (2021) found that shallow cumulus clouds are thicker at night, and the radiative effects could potentially play an important role. The surface wind speed is also often stronger at night, driving stronger surface latent heat flux (LHF) that deepens the cloud layer (Nuijens & Stevens, 2012; Vial et al., 2021).

The depth of shallow cumulus clouds and its variation also depend on whether the clouds precipitate. Vial et al. (2019) found that non-precipitating shallow cumuli grow during the day and reach the maximum vertical extent during sunset. On the other hand, precipitating shallow cumuli grow deeper at night with a maximum before sunrise. Vial et al. (2021) further shows that different mesoscale organization states also occur at different times of the day and can affect both the cloud depth and cloud fraction. Gravel and flowers often occur at night in deeper boundary layers, while sugar and fish are often observed during the day when the boundary layer is shallower. A change in cloud organization pattern contributes more to the daily variation of cloud fraction and cloud depth than the diel cycle of the same cloud organization pattern.

Aerosol can also modulate the radiation and indirectly affect the cloud properties. The aerosol-radiation interactions alter the planetary albedo, further changing the conditions of the boundary layer in which shallow clouds are formed. Multiple field campaigns were conducted to study the cloud-radiation and aerosol-radiation interactions in the past decade. The Cloud Systems Evolution in the Trades (CSET) field campaign used the National Science Foundation and National Center for Atmospheric Research Gulfstream V (HIAPER) to study the evolution of the boundary layer aerosol, cloud, and thermodynamic structures in the tradewind regions over the North Pacific Ocean in July-August 2015 (Albrecht et al., 2019). The Layered Atlantic Smoke Interactions with Clouds (LASIC) used the surface-based observations from the Atmospheric Radiation Measurement (ARM) Mobile Facility (AMF) to study tradewind shallow cumuli near Ascension Island offshore of Africa between July 2016–October 2017 (Zuidema et al., 2018). The most recent field campaign that combined the studies of shallow cumulus clouds, aerosol, boundary layer structure, and large-scale meteorological and oceanic conditions altogether was the U.S. Atlantic Tradewind Ocean-Atmosphere Mesoscale Interaction Campaign (ATOMIC) and the European multinational Elucidating the Role of Clouds-Circulation Coupling in Climate field observation (EUREC[4]A), which took place in January–February 2020, over the Atlantic Ocean near Barbados (Bony et al., 2017, 2022; Pincus et al., 2021; Quinn et al., 2021; Stephan et al., 2021; Stevens et al., 2021).

During the ATOMIC and EUREC^{4}A field campaigns, there were several days when mineral dust, black carbon, biomass burning, and other aerosol species were observed in the region, enabling studies of the interactions between clouds and aerosol (Bony et al., 2022; Quinn et al., 2021). The four mesoscale organization patterns of shallow cumuli were observed throughout the field campaign period, and transitions between the cloud patterns took place (Bony et al., 2022; Narenpitak et al., 2021; Pincus et al., 2021; Schulz, 2021; Stevens et al., 2021). In particular, on 2–3 February 2020, a transition from sugar to flower shallow cumulus clouds was observed near Barbados over the course of less than 24 hr. Between January 31 and February 3, an aerosol layer consisting mainly of mineral dust was observed above the clouds, resulting in an aerosol optical depth of approximately 0.35 (Quinn et al., 2021). Narenpitak et al. (2021) simulated this sugar-to-flower (S2F) transition event and determined the mechanism of the transition using the System for Atmospheric Modeling (SAM) as a large eddy simulation (LES), driven with reanalysis data based on the approach in Kazil et al. (2021). In Narenpitak et al. (2021), the mechanism responsible for the S2F transition is the mesoscale circulation associated with the shallow cumulus plumes that renders the moist and cloudy areas moister, and dry areas drier. The organization is strengthened further when the cloud system experiences stronger large-scale upward motion, as a deeper cloud layer is accompanied by stronger mesoscale circulation that accelerates the organization.

Using the results from LES together with the ship-based measurements, Narenpitak et al. (2021) quantified the amount of surface radiation flux modulated by the mineral-dust layer at the location of the National Oceanic and Atmospheric Administration's (NOAA) Research Vessel Ronald H. Brown (RHB), which was stationed at 54.5°W and 13.0°N during the dusty period. The mineral dust reduces the amount of downward solar radiation reaching the RHB (their Figure A3). This work extends Narenpitak et al. (2021) to study the cloud-radiation interaction and the aerosol-radiation interaction in the context of the S2F transition. The first part examines the role of the diel cycle on the S2F transition, precipitation, and the cloud and cold pool dynamics. The second part examines the role of free-tropospheric mineral dust on radiation and its impacts on the transition and organization of the clouds.

The organization of this paper as follows. Section 2 describes the configuration of the simulations and the data used from the field campaign. Section 3 describes mathematical equations used to quantify the strength of cloud organizations and to detect the cold pools. Section 4 analyses the impacts of the diel cycle on the S2F transition. Section 5 explores the impacts of free-tropospheric mineral dust on the clouds. Finally, Section 6 presents the conclusions.

2. Data and Simulations

The System for Atmospheric Modeling or SAM (Khairoutdinov & Randall, 2003) is employed to simulate the transition from sugar to flower shallow cumuli observed on 2–3 February 2020, during the ATOMIC and EUREC^{4}A field campaigns. The simulations are driven with the large-scale forcings from the European Center for Medium-Range Weather Forecasts (ECMWF) Reanalysis Fifth Generation (ERA5) (Hersbach et al., 2020), following a boundary-layer air mass that passes over the RHB at 13:00 local time (17 UTC) on 2 February 2020. The trajectory was calculated by the Hybrid Single-Particle Lagrangian Integrated Trajectory (HYSPLIT) model (Rolph et al., 2017; Stein et al., 2015) with the initial point from the RHB at 500 m altitude forward and backward in time to construct a time-height curtain of the large-scale atmospheric conditions. The greenhouse gas concentration profiles of carbon dioxide, methane, nitrous oxide, and ozone are based on the Community Earth System Model version 1 (CESM1) (Hurrell et al., 2013) Whole Atmosphere Community Climate Model (WACCM; Marsh et al., 2013). The ensemble-mean outputs are from the CESM1-WACCM simulations initialized following the representative concentration pathway 8.5 (RCP8.5, a high anthropogenic emission scenario). The greenhouse gas concentration profiles averaged from January–February of 2016 through 2025 over 10.42°N–21.79°N and 295°E–310°E are used to represent the current climate over the Atlantic Ocean. Unless otherwise noted, the other details of the simulation configurations are as described in Section 2 of Narenpitak et al. (2021).

Three simulations are presented in this paper, as summarized in Table 1. All of them are configured with horizontal grid spacing of 100 m and a horizontal domain extent of 192×192 km^2. The vertical grid spacing is 50 m, increasing geometrically from 5 to 10 km, which is the domain top. There are 125 vertical levels in total. Above the model top, the atmospheric profiles from ERA5 and greenhouse gas concentrations from CESM1-WACCM are used up to the top of the atmosphere for the radiation calculation. As in Narenpitak et al. (2021), the simulations use a two-moment bin-emulating bulk microphysics scheme (Feingold et al., 1998) and the Rapid Radiative

Table 1
Major Configuration Differences in the Three Sugar-To-Flower (S2F) Transition Simulations

Simulations	Time of the cloud transition	Timing of the solar radiation	Mineral dust
Control	Control	Directly from ERA5 (22:00–22:00 local time)	None
Diel+12h	Diel+12h	Shifted 12 hr later from ERA5 (10:00–10:00 local time)	None
Dust	Control	Directly from ERA5 (22:00–22:00 local time)	Initialized between 4 and 5.5 km (1,600 mg^{-1} concentration, AOD $\approx$ 0.35)

Transfer Model for global climate model applications (RRTMG) (Mlawer et al., 1997) with time varying atmospheric profiles above the domain top and the diel cycle of solar radiation. The radiation is computed every 10 s. The model time step is 2 s, and the duration of the simulations is 24 hr.

The primary aerosol type in all of these three simulations is sea-salt particles. The simulations are initialized with a bimodal sea-salt aerosol distribution in the boundary layer, based on the shipboard measurement from the RHB (Quinn et al., 2021). The sea-salt aerosol size distribution is shown in Figure A2 of Narenpitak et al. (2021). The fine mode sea-salt aerosol (with a geometric mean diameter of 0.13 μm and a geometric standard deviation of 1.71) has a concentration of 400 mg^{-1}, and the coarse mode aerosol (with a geometric mean diameter of 0.96 μm and a geometric standard deviation of 1.73) has a concentration of 13 mg^{-1}. The initial sea-salt aerosol concentration in the free troposphere is 32 mg^{-1}, consistent with the EUREC[4]A measurements from the Ultra-High-Sensitivity Aerosol Spectrometer (UHSAS) and the Cloud Droplet Probe (CDP-2) on the French ATR-42 research aircraft (Bony et al., 2022; Coutris & Ehses, 2021). The sea-salt particles are coupled with the cloud microphysics scheme.
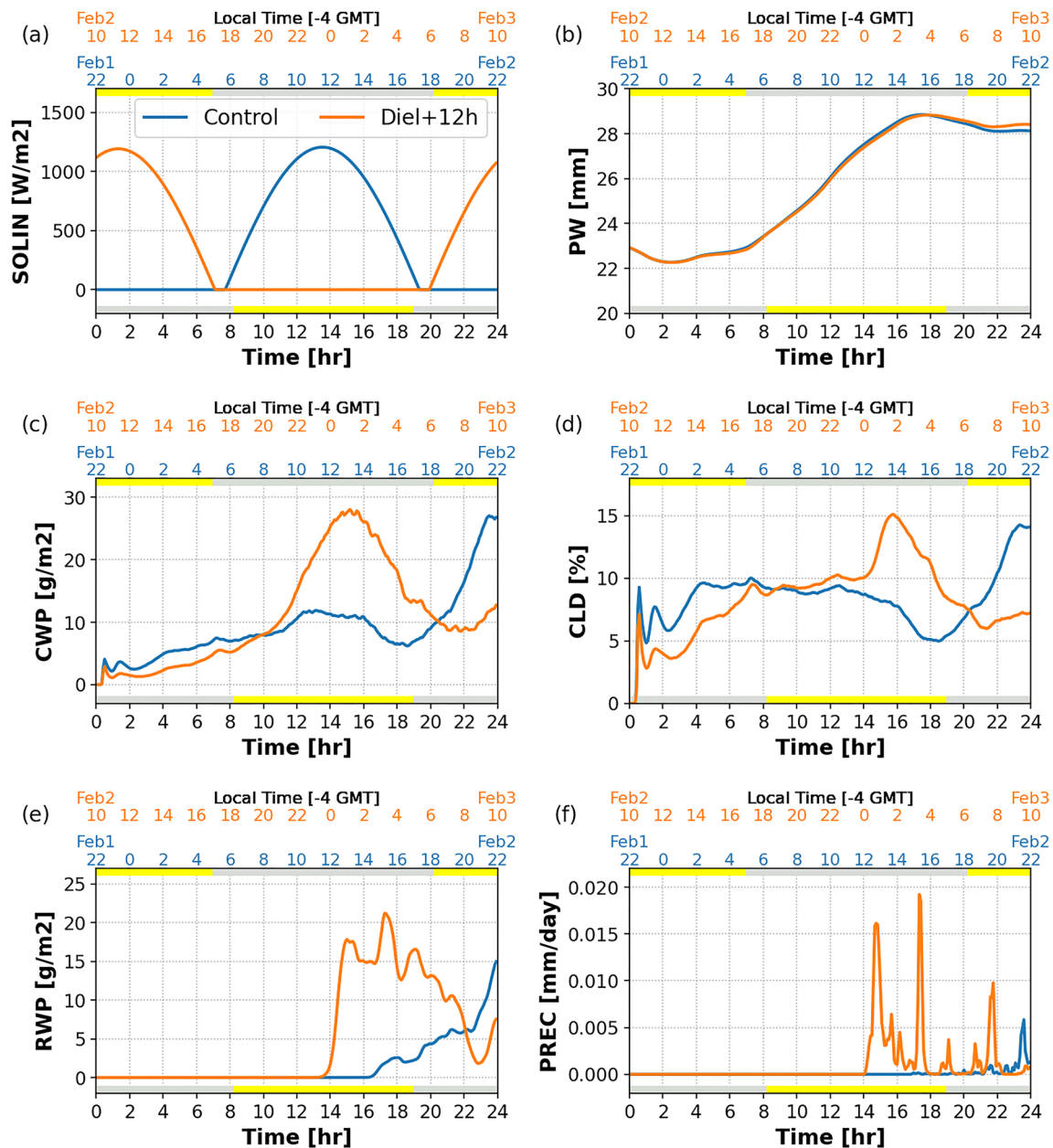
2.1. The Control and Diel+12h Simulations

Two simulations are used to assess the impact of the diel cycle on the S2F transition: the Control and the Diel+12h simulations. The Control simulation represents the S2F transition observed on 2–3 February 2020, except without a mineral-dust layer initialized in SAM. The diel cycle in the Control simulation follows that of ERA5, and the insolation, computed from RRTMG, is shown in Figure 1a (blue line). The S2F transition occurred between hours 10 and 18 of the simulation or 8:00 to 16:00 on February 2 local time. The Control simulation is run from 22:00 on February 1 to 22:00 on February 2, local time.

The Diel+12h simulation examines the impact of the diel cycle on the S2F transition, as if the transition had occurred at night. The time variable in the forcing file is, therefore, delayed by 12 hr (Figure 1a, orange line), so the simulation is run from 10:00 on February 2 to 10:00 on February 3, local time. Aside from the shifted diel cycle, everything else from the large-scale meteorology of ERA5 remains the same. The results of these two simulations are presented in Section 4.

2.2. The Control and Dust Simulations

Two simulations are used to assess the impact of mineral dust in the free troposphere on the S2F transition: the Control and Dust simulations. The Dust simulation examines the radiative impacts of the mineral dust on the moisture aggregation and the transition of the clouds. Between 2–3 February 2020, a layer of mineral dust advected from Africa over to the Caribbean was observed above the cloud layer near Barbados (Bony et al., 2022; Quinn et al., 2021). To represent the observed dust layer, an additional aerosol species is included in SAM. A mineral-dust layer with a concentration of 1,600 mg^{-1} is initialized between 4 and 5.5 km, colocated with an elevated moist layer (EML), as described in Appendix A2 of Narenpitak et al. (2021). A SAM simulation that has the same model configuration as the Dust simulation in this study is able to represent the vertical structure of the specific humidity (QV) observed by the radiosonde profiles from the RHB Research Vessel (Figure 1b of Narenpitak et al. (2021)). For this particular case, the enhanced QV in the EML is approximately 2 g kg^{-1}, smaller than the observed enhanced QV in previous studies (i.e., Gutleben, Groß, Wirth, Emde, and Mayer (2019) and other references therein).

Figure 1. Domain-mean time series of various variables from the control simulation (Control, blue) and the simulation with a 12-hr delay in the diel cycle (Diel+12h, orange): (a) insolation, (b) precipitable water, (c) cloud water path, (d) cloud fraction, (e) rain water path, and (f) surface precipitation. The bottom x-axes indicate time after the simulations begin, while the top x-axes indicate the local time of both simulations, relative to the insolation. Other large-scale forcings are kept identical. The gray band indicates the night and the yellow band indicates the day (insolation greater than zero). The bottom band is for the Control simulation, and the top Diel+12h.

The mineral dust optical properties are calculated based on the assumed size distribution and refractive indices in d'Almeida et al. (1991). The dry aerosol single scattering albedo is 0.85 in the visible part of the spectrum. The aerosol optical depth at this time is approximately 0.35, consistent with the Moderate Resolution Imaging Spectroradiometer (MODIS) observation at this time. The mineral dust is advected in all directions and allowed to spatially and temporally vary the radiative heating rate. The local heating rate of the mineral dust is computed using a look up table of wavelength dependent optical properties (single scattering albedo, asymmetry parameter, and extinction coefficient) of dry mineral dust aerosol with the size distribution measured during ATOMIC (Quinn et al., 2021). The assumption of dry particles is consistent with the low (<15%) relative humidity in the free troposphere in the simulations, where the mineral-dust layer is located. The mineral dust is coupled with

the radiation scheme, but not with the cloud microphysics scheme, because the mineral-dust layer resided above the boundary layer.

In addition to the original output variables from SAM, the radiative fluxes and radiative heating rates (both solar or shortwave and infrared or longwave radiation) from the atmosphere without mineral dust are also calculated. Thus, the radiative heating due to the mineral dust can be directly obtained by subtracting the total radiative fluxes (and heating rates) from those of the atmosphere without mineral dust. These variables are useful for determining the effects of the mineral dust on the radiation and the moisture aggregation in Section 5.

3. Methods

3.1. Scale Partitioning

Narenpitak et al. (2021) examined the mechanism responsible for the moisture aggregation in their simulations. Following Bretherton and Blossey (2017), the simulation output is partitioned into contributions from the large scale, mesoscale, and cumulus scale. The scale partitioning can be performed on any variable fields. Consider, for example, the vertical velocity output at a particular time $w(x, y, z, t)$; the partitioning of vertical velocity is given by:

$$w(x, y, z, t) = \overline{w}(z, t) + w''(x_m, y_m, z, t) + w'''(x, y, z, t). \tag{1}$$

The over-line indicates the domain average, representing the large-scale contribution. The double prime indicates the perturbation from the domain average, coarse-grained to a tile size that is representative of the mesoscale (x_m, y_m), such as 16 km. The quantity represents the variability associated with the mesoscale perturbation. The triple prime term is the residual, which represents the variability associated with the cumulus-scale process. Unless otherwise specified, the tile size of 16 km is used for coarse-graining and computing the mesoscale contribution. Readers are referred to Section 3.1 and Appendices B and D1 of Narenpitak et al. (2021) for details.

The term $w''(x_m, y_m, z, t)$ represents the mesoscale vertical velocity perturbation relative to the domain average. When positive, $w'' > 0$ indicates that there is local (mesoscale) ascent in the considered mesoscale tile. Mass continuity requires that there is local convergence below and local divergence aloft in the areas where $w'' > 0$. The w'' profiles can be sorted by the total water path (TWP, a sum of water vapor, cloud water and rain water paths) at every time step, and averaged into quartiles of TWP. The lowest TWP quartile (Q1) represents the driest and cloud-free regions; whereas the highest TWP quartile (Q4) represents the moist and cloudy regions. The mesoscale tiles in these quartiles are not necessarily adjacent to one another.

3.2. The Mesoscale Total Water Perturbation Budget

As found in Bretherton and Blossey (2017) and Narenpitak et al. (2021), the mesoscale circulation mentioned above is responsible for aggregating the total water in the non-precipitating shallow cumuli, rendering the moist areas moister and the dry areas drier. The process can be mathematically explained using the budget of mesoscale total water perturbations or q_t'':

$$\frac{\partial q_t''}{\partial t}(x_m, y_m, z, t) = \mathcal{A} + \mathcal{F} + \mathcal{C} + \mathcal{S}. \tag{2}$$

It consists of four main processes: the advection of q_t'' due to the large-scale and mesoscale winds ($\mathcal{A}$), the horizontal and vertical gradients of the cumulus-scale total water flux ($\mathcal{F}$), the mesoscale vertical advection of large-scale total water ($\mathcal{C}$), and the mesoscale perturbations of the precipitation mass flux divergence ($\mathcal{S}$). The details are described in Appendix B.

Bretherton and Blossey (2017) found that $\mathcal{C}$ dominates the q_t'' budget of shallow cumulus organization in the Pacific Ocean. Narenpitak et al. (2021) further found that, although the S2F transition is a different cloud regime than those observed over the Pacific Ocean, $\mathcal{C}$ still dominates the q_t'' budget in the non-precipitating flower aggregates observed over the Atlantic.

The $\mathcal{C}$ term will be referred to and shown throughout the rest of this paper. Because of mass continuity, the mesoscale vertical advection of the large-scale total water,

$$C = -w'' \frac{\partial \overline{q_t}}{\partial z}, \tag{3}$$

can be physically interpreted as a mesoscale convergence or divergence (as represented by w'') of the large-scale total water gradient $\left(\frac{\partial \overline{q_t}}{\partial z}\right)$. Since the large-scale total water $\overline{q_t}$ decreases with height, it follows that $C > 0$ when $w'' > 0$, or when there is local convergence below and divergence aloft. When C is vertically integrated, it represents the net convergence or divergence of total water. If $\int C \mathrm{d}z > 0$, there is net convergence of total water in the considered mesoscale region, which will then become moister with time.

3.3. Organization Diagnostics

There are multiple ways to quantify the strength of shallow convection organization, including but not limited to comparing the distance of the nearest clouds, which is often expressed as an index called I_{org}, comparing the cloud cluster sizes, and the variance of the moisture fields (Bony et al., 2020; Bretherton & Blossey, 2017; Tompkins & Semie, 2017). Three organization diagnostics are used in this paper: the mean area of cumulus aggregates, the cloud aggregate counts, and the normalized standard deviation of TWP. An algorithm is developed to detect the aggregates of adjacent cloudy pixels with the total (cloud and rain) optical depth exceeding 1. The area of the cloud aggregates is, therefore, a factor of the simulation grid size or 100×100 m^2. Larger cloud aggregate areas and fewer aggregate counts mean the mesoscale organization is stronger. The normalized standard deviation of TWP is the ratio of the TWP standard deviation (σ_{TWP}) divided by the domain-mean TWP $\left(\overline{TWP}\right)$. Greater normalized TWP standard deviation also implies stronger organization, as the dry areas become drier and the moist areas become moister.

3.4. Cold Pool Detection

Shallow cumulus cold pools are regions of colder air, surrounded by warmer air, associated with evaporative downdrafts of significant precipitation from shallow cumulus clouds (Rauber et al., 2007; Zuidema et al., 2017). As the cold air reaches the surface, it creates a density current pushing the air outward forming a mesoscale circular edge. The air along the gust front can create a second cycle of convection, forming new clouds at the edge of the cold pools. With this definition, a sharp drop in the near-surface or subcloud-layer temperature is used to identify the cold pools.

Cold pools are found in all of these three simulations after precipitation onset. In this study, cold pools are detected using a threshold of the surface virtual potential temperature (Θ_v), a similar approach as in Touzé-Peiffer et al. (2022). The threshold computed using the instantaneous output of Θ_v at the respective time is:

$$\tilde{\Theta}_v - \sigma_{\Theta_v},$$

where $\tilde{\Theta}_v$ is the median of the surface Θ_v in the entire domain, and σ_{Θ_v} is the standard deviation of the surface Θ_v within the domain. Any grid cell with Θ_v below the threshold is considered part of the cold pools.

The cold pools can also be determined by the surface divergence and convergence. The surface divergence term (Div) is computed from 2-km coarse-grained horizontal wind fields at the surface:

$$Div = \left[\frac{\partial u_s}{\partial x}\right]_{2km} + \left[\frac{\partial v_s}{\partial y}\right]_{2km}. \tag{4}$$

The areas in which $Div > 1 \times 10^{-6}$ s^{-1} are in precipitating downdrafts. The contours where $Div < -1 \times 10^{-6}$ s^{-1} indicate areas where there is strong surface convergence associated with the gust front or the cold pool edges. Cold pools with stronger downdrafts and surface divergence are often associated with a deeper temperature drop (Vogel et al., 2021). See Figures 3, 4, and 10 for examples.
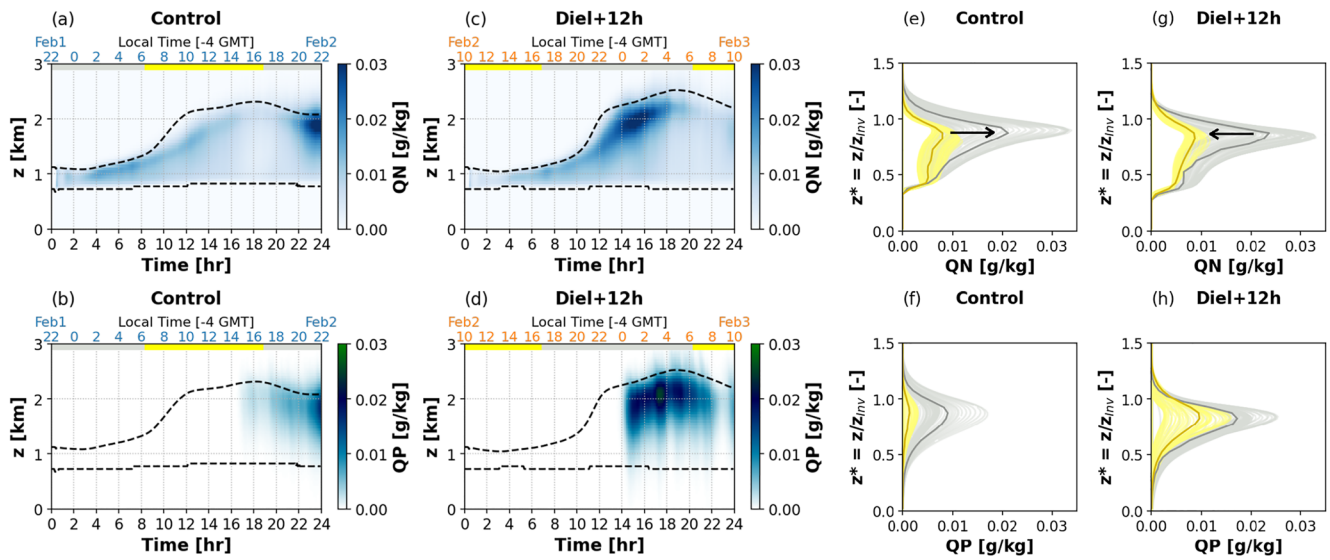
Figure 2. Domain-mean time series and vertical profiles of (top) cloud water mixing ratio (QN) and (bottom) rain water mixing ratio (QP) from the Control and Diel+12h simulations. (a, b) Time series of QN and QP from Control; the lower x-axes indicate time after the simulations begin and the upper x-axes indicate the local time of the Control simulation. The gray and yellow band indicate nighttime and daytime, respectively. (c, d) As in panels (a, b) but for the Diel+12h simulation. (e, f) Vertical profiles of domain-mean QN and QP from Control after 14 hr (last 10 hr of the simulations) composited and plotted against the normalized height (z^*), which is the ratio between the physical height (z) and the domain-mean inversion height (z_{Inv}) of the respective simulations. The yellow (gray) profiles are from the day (night). The average profiles from the day (night) are plotted in dark yellow (dark gray). Panels (g, h) are as in (e, f) but for the Diel+12h simulation. The black arrows in panels (e and g) point from the earlier times (lower precipitable water (PW)) to the later times (higher PW).

## 4. The Impacts of the Diel Cycle on the S2F Transition

4.1. The Diel Cycle and the Transition From Sugar to Flowers

This section focuses on the impact of the diel cycle on the S2F transition. Figure 1 shows the evolution of the shallow cumulus clouds in the Control (blue) and Diel+12h (orange) simulations. Prior studies found that at night, the surface wind speed of the shallow cumulus clouds is often stronger than during the day, leading to stronger surface LHF, deeper clouds, and higher cloud amount (Nuijens & Stevens, 2012; Vial et al., 2021). For the Control and Diel+12h simulations, the surface wind speed is kept identical (Figure A1a) to eliminate the potential consequences of this factor. Figures 1c–1f shows that the Diel+12h simulation produces more cloud and rain water than Control. Although the precipitable water (PW, or the column integrated water vapor) gradually increases from hours 6 to 16, the cloud and rain water are maximized at night in each simulation, regardless of the surface wind speed, surface latent and sensible heat fluxes, and the Bowen ratio (Figure A1).

Figures 2–4 show that the S2F transition in the Diel+12h simulation occurs more rapidly than the transition in Control. In both simulations, the cloud layers are both initially shallow. They similarly deepen rapidly during hours 10–12 because of a strong upward motion in the large-scale forcings (Figure 3b in Narenpitak et al. (2021)). The maximum cloud top height is slightly higher in the Diel+12h simulation, and the cloud tops reach their maximum heights during hours 16–18 in both simulations. The cloud and rain amounts in the Diel+12h simulation reach their maximum values 12 and 6 hr sooner, respectively, compared to the Control simulation (Figures 2a–2d). The snapshots of the cloud fraction (CLD) and TWP in Figures 3 and 4 show that as the aggregated flower clusters precipitate, the cloud system produces a large number of cold pools beneath the clouds. The Diel+12h simulation, which has stronger precipitation, also produces more cold pools.

The results so far clearly show that the Diel+12h simulation produces larger flower clusters with more cloud liquid water and rain, with the only factor that is different between the Diel+12h and Control simulations being the timing of the solar radiation. This is summarized by Figures 2e–2h. The domain-mean output in the last 10 hr of both simulations are composited and plotted against the normalized height (z^*), which is the altitude (z) divided by the domain-mean inversion height (z_{Inv}) at each time. The yellow (gray) profiles are from the day (night). The cloud liquid water and rain water of the aggregated shallow cumuli are greater at night, regardless of the large-scale water vapor in the forcings. The clouds are in a larger form of flower aggregates, as shown in the
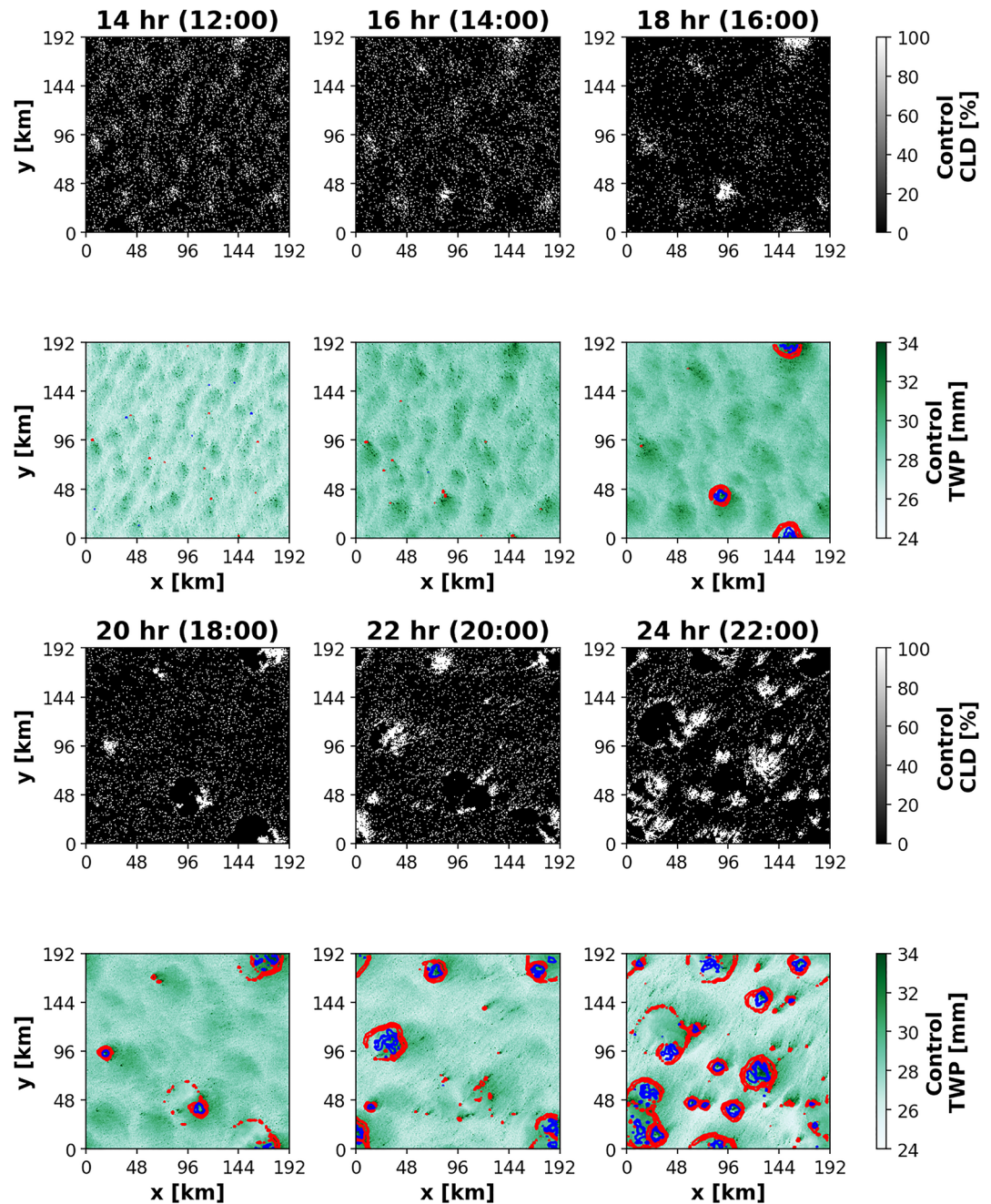
Figure 3. Snapshots of (top) cloud fraction (CLD) and (bottom) total water path (TWP, which is a sum of water vapor, cloud and ran water paths), showing the transition from sugar to flower shallow cumuli from the Control simulation. The snapshots are plotted every other hour during the last 12 hr of the simulation (12:00 to 22:00, local time). The red and blue contour lines on the TWP snapshots show areas where the magnitudes of surface convergence (red contours) and surface divergence (blue contours) are stronger than $10^{-6}\,\mathrm{s}^{-1}$. The areas with surface divergence correspond to the precipitating downdrafts associated with the clustered shallow cumuli and the rings of surface convergence correspond to the edges of cold pools.

domain snapshots (Figures 3 and 4) and the mean area of the cloud aggregate time series (Figure 5a), and have larger cloud water mixing ratio at the top of the cloud layer, which is a key characteristic of the flower clouds (Bony et al., 2020). This feature is consistent with previous studies, such as Vial et al. (2019); Vial et al. (2021) who showed that shallow cumuli are often deeper at night when the shortwave radiative heating is zero. Since the only difference in the model configuration is the shifted diel cycle, this study emphasizes that the solar radiation alone has a strong influence on the shallow cumulus cloud system.
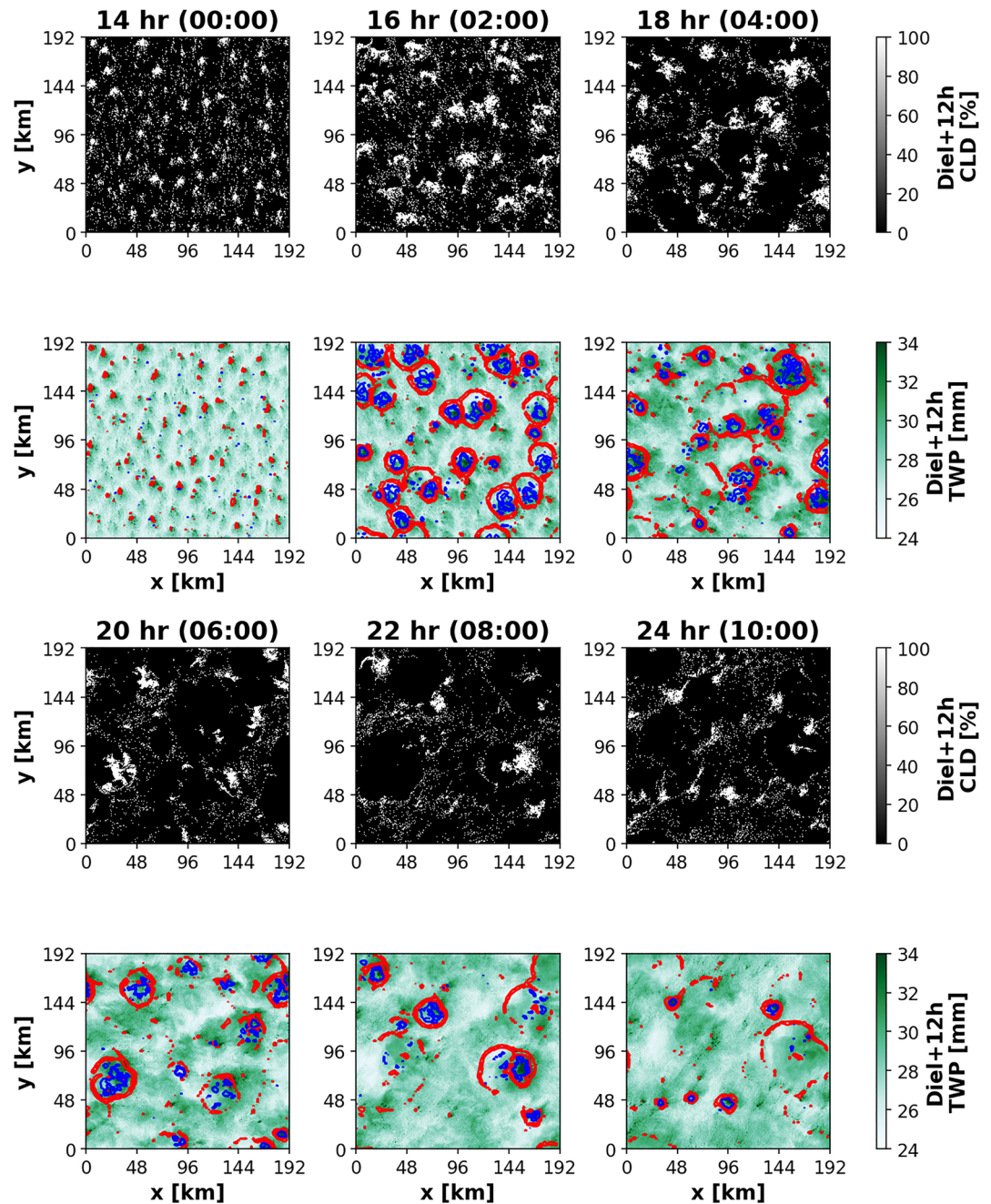
Figure 4. As in Figure 3 but for the Diel+12h simulation. The snapshots are from 0 to 10 a.m., local time.

The solar radiation not only affects the domain-mean quantities of the simulations but also has a strong influence on the distribution of moisture and clouds. Figures 3 and 4 show that the clouds and the total water in both simulations have aggregated into clusters surrounded by dry regions, especially in the second half of the simulation despite weaker surface wind speed. The clouds in the Diel+12h simulation aggregate sooner than those in the Control simulation. As the clouds grow, they produce sufficient rain water, resulting in precipitating downdrafts that generate cold pools. The edges of the cold pools are indicated by red contours, which represent areas where convergence of the surface horizontal wind is stronger than 10^{-6} s^{-1}. The moisture aggregation is strongest and the cold pools are the most dense at night.
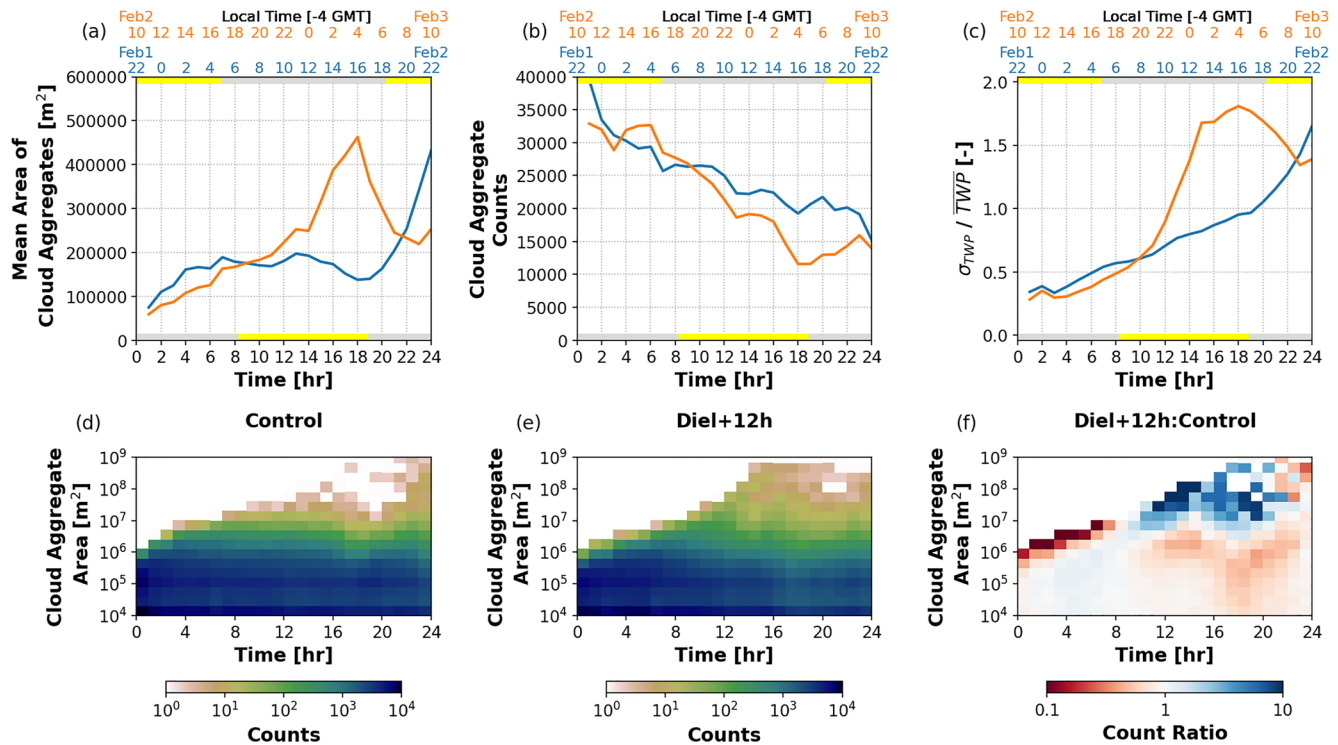
Figure 5. Time series of (a) the mean area of cumulus cloud aggregates, with a contiguous cloud optical depth exceeding 1 (QOPD >1), (b) the cloud aggregate counts, and (c) the standard deviation of total water path (TWP) normalized by the domain-mean TWP from the Control (blue) and Diel+12h (orange) simulations. The x-axis labels are as in Figure 1. (d, e) Hourly distributions of the cloud aggregate areas from the Control and Diel+12h simulations, plotted against time. (f) Ratio of the distributions of the cloud aggregate areas between the Diel+12h and Control simulations. When the ratio is greater than one, the Diel+12h simulation produces more aggregates of the respective cloud sizes than the Control simulation.

4.2. The Diel Cycle and the Mesoscale Aggregation of Moisture and Clouds

Figures 5a–5c shows the hourly time series of various organization diagnostics: (a) the mean area of cloud aggregates, (b) the cloud aggregate counts, and (c) the normalized TWP standard deviation of both simulations. The time series clearly show that in the early morning, the Diel+12h simulation produces the largest mean area of cloud aggregates (maximum of 450,000 m^2, or 45 pixels, at hour 18 or 4:00 local time) and the lowest aggregate counts (slightly above 10,000 aggregates). The normalized TWP standard deviation also increases rapidly and remains higher at night. These indicate the time of strongest mesoscale organization in the Diel+12h simulation. On the other hand, the Control simulation takes longer to reach a similar maximal organization strength after hour 22, as it needs not only sufficient PW to produce clouds but also suffers from the boundary layer warming in response to absorption of shortwave radiation in the afternoon which hinders cloud deepening.

The distributions of the cloud aggregate areas plotted every hour are displayed in Figures 5d and 5e, and the ratio of both histograms (Diel+12h to Control) in Figure 5f. The ratio of the Diel+12h to Control cloud aggregate area distributions suggest that, at night, between hours 8 and 22, the Diel+12h simulation produces higher cloud aggregate counts with areas larger than $5 \times 10^6 \, m^2$, or 500 pixels. This clearly shows that the diel cycle has strong impacts on the rate of moisture aggregation in the mesoscale.

Figure 6 shows vertical profiles of the mesoscale vertical velocity perturbation relative to the domain averages (w'') and the convergence of total water due to mesoscale circulation (C, see Equations 2 and 3). They are sorted by TWP and averaged into quartiles of TWP at respective times. The highest TWP quartile or Q4 represents the top 25% of the moistest and cloudiest regions in the Control and Diel+12h simulations (dark blue lines). The time-height curtains of C from the highest TWP quartile are shown at bottom. The vertical profiles of w'' from the Control simulation (Figures 6a–6e, dashed lines) are consistent with the finding in Figure 4 of Narenpitak et al. (2021). As the sugar clouds transition into the flower clouds, there is local ascending (descending) air in (above) the mesoscale cloud plumes, and local descending air in the surrounding dry regions. Mass continuity
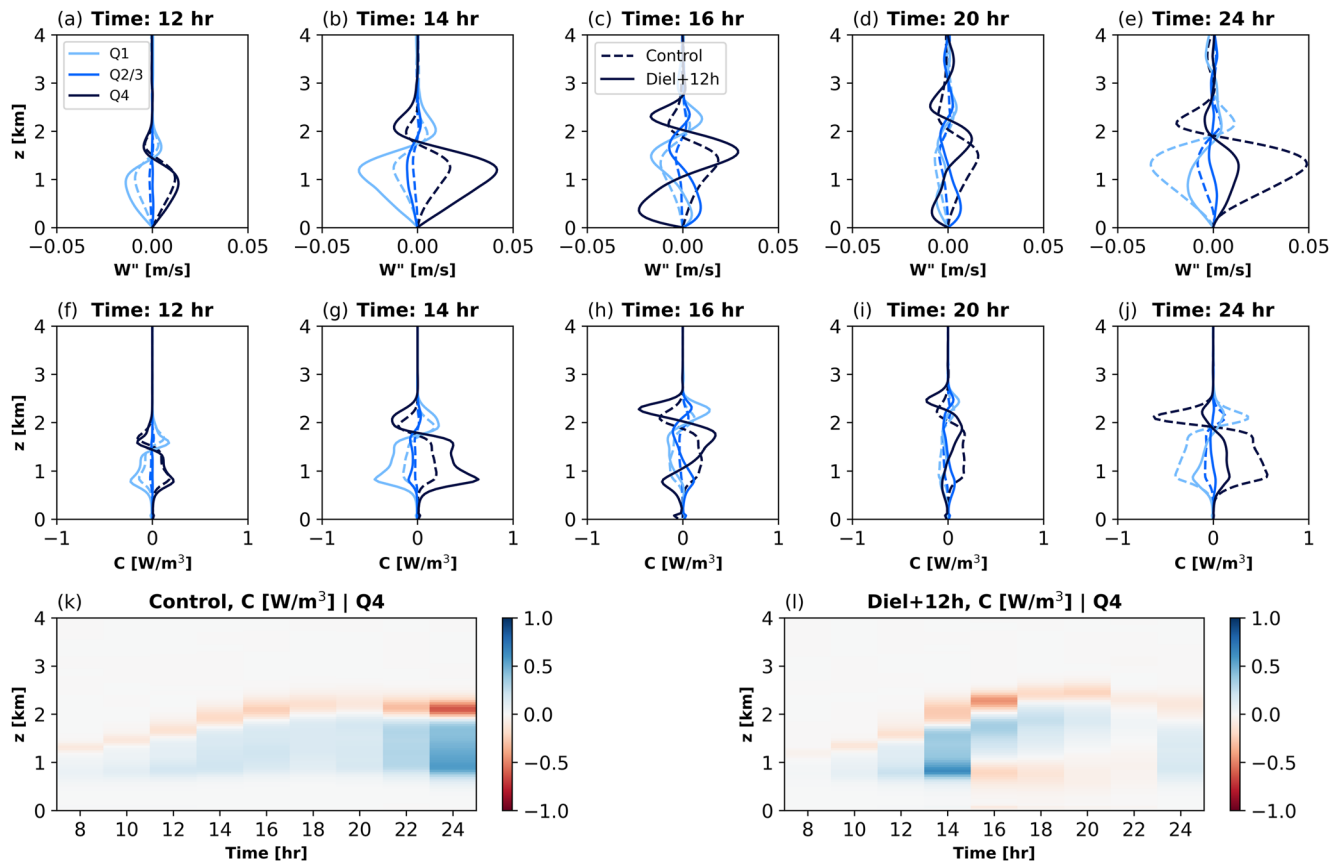
Figure 6. Vertical profiles of (a–e) the mesoscale perturbation of vertical velocity from the domain averages (w'') and (f–j) the moisture convergence due to mesoscale circulation (C) from the Control and Diel+12h simulations, plotted at various times. The profiles are sorted by the total water path (TWP) or TWP at the respective times and averaged into four TWP quartiles, Q1 being the lowest quartile (driest, light colors) and Q4 being the highest (moistest, dark colors). The profiles from Q2 and Q3 are averaged. (k, l) Time-height curtains of C from the highest TWP quartile from the Control and Diel+12h simulations.

implies that there is local convergence below the mesoscale cloud plumes, and local divergence above. Further analysis of the mesoscale total water perturbation (q_t'') budget shows that there is an overall convergence of total water in the cloud layer of the already moist and cloudy regions of the Control simulation ($C > 0$), allowing the moisture aggregation to strengthen and the cloud clusters to grow (Figures 6f–6j and 6l). See Appendix B and Figure B1 of this paper for the other terms in the q_t'' budget equation.

In contrast, the results from the Diel+12h simulation show that the simulation has a higher C in the entire boundary layer at hour 14. After this, the clouds reach their maximum depth and start to precipitate more, limiting the cloud growth. When the shallow cumuli are heavily precipitating (hours 16–20), the convergence of total water due to mesoscale circulation computed at a 16-km mesoscale tile is negative in the subcloud layer. The w'' and C terms are still positive in the cloud layer of Q4, suggesting that there is still local convergence of moisture into the cloud plumes. But the surface divergence beneath the clouds removes the moisture from the moist regions below the cloud plumes. This is shown in Figures 6h–6i and 6l.

An argument can be made that the C term is still responsible for moistening the moist columns, but over a smaller scale. Instead of using 16 km, the scale of the moist columns needs to be adjusted such that they are smaller than the size of the cold pools to see this effect. The column-integrated mesoscale moisture convergence is negative between hours 16–20 in Q4 when a 16-km tile size is used for the q_t'' budget (Figures 6h–6i). However, it is still positive if smaller tile sizes (6.4 km or smaller) are used (Figure B4d). Figures B4 and B5 show that, at the center of the cold pools where precipitating downdrafts are present, the mixed-layer total water divergence ($C < 0$) is compensated by the upward vertical advection of total water perturbations $\mathcal{A}_v > 0$. At the edges of the cold pools, there is mixed-layer total water convergence ($C > 0$). The moisture influx and the dynamical lifting at the edges of the cold pools assist in initiating a new generation of flower clouds. This is consistent with the snapshots of the
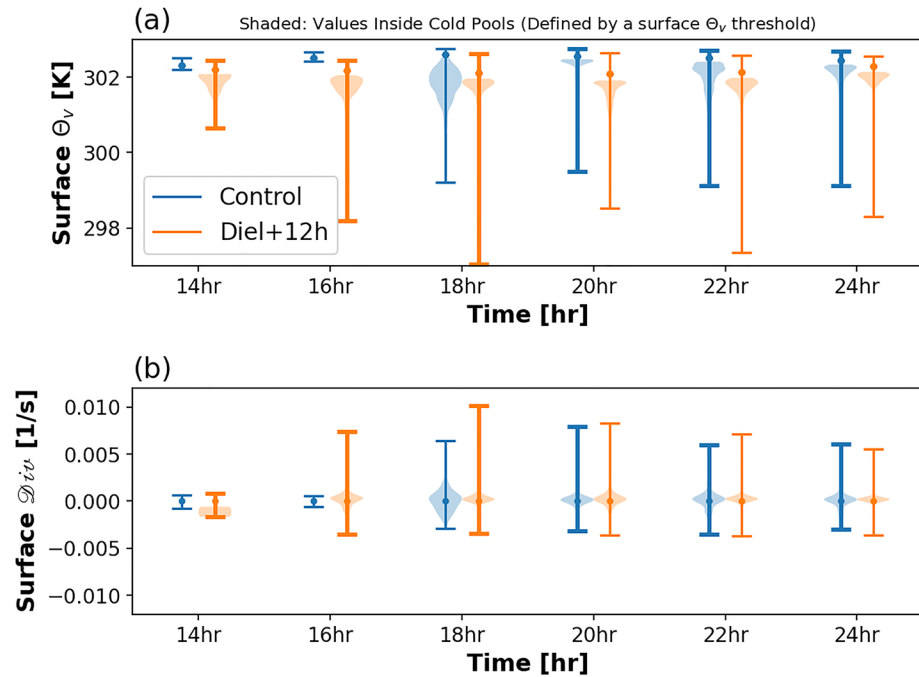
Figure 7. Distributions of (top) the surface virtual potential temperature (Θ_v) and (bottom) the surface divergence term (Div) every 2 hours from the Control (blue) and Diel+12h (orange) simulations. The thick lines indicate nighttime, thin lines daytime. The shaded areas show the distributions (by density) of surface Θ_v and Div inside the cold pools. The short horizontal lines represent the minima and maxima, and the dots represent the medians. The histograms are plotted every 2 hr from hours 14 to 24.

Diel+12h simulation at hours 16–18 (Figure 4). As the new convection takes place, the old cold pools dissipate. These cloud and cold pool interactions observed in the Diel+12h simulation are consistent with previous findings (Zuidema et al., 2012, 2017). The fact that the near-surface C term has opposite sign when different mesoscale tile sizes are used (16 vs. 6.4 km) suggests that sufficient horizontal resolution is important for representing processes associated with cloud and cold pool dynamics.

The precipitating downdrafts inside cold pools are associated with the influx of air, with low virtual potential temperature from above, toward the surface. Figure 7 further elucidates the interactions of cloud, cold pool, and precipitation, and the differences that occur between night and day. The distributions of (a) the surface virtual potential temperature (Θ_v), and (b) the surface divergence (Div) (see Equation 4) are presented. The surface Θ_v term is used as a proxy for the surface buoyancy; lower surface Θ_v means less buoyancy and stronger cold pools (Vogel et al., 2021). The positive Div term represents the strength of the precipitating downdraft and the gust front, a density current that carries the moisture outward, lifting the air in the mixed layer, forming new convection (Zuidema et al., 2012). The shaded areas show Θ_v and Div inside the cold pools. The distributions are shown starting from hours 14, when significant precipitation generates cold pools in the Diel+12h simulation. It is clear that cold pools developed in the Diel+12h simulation are stronger, even when compared with the cold pools that develop at night of the Control simulation. The associated gust fronts also lead to new convection that grows into a second generation of flower clouds that later precipitate and also form new cold pools.

4.3. Discussion

So far, this study examines the transition of shallow cumulus clouds from the sugar state to the flower state of organization. During the course of less than 24 hr, the clouds deepen and the organization becomes stronger despite weaker surface wind speed in the latter half of the simulation. A sensitivity test shows that in the absence of solar radiation, as the cloud layer deepens, the S2F transition is accelerated and the organization becomes stronger.

Regardless of when the transition takes place, the mesoscale moisture convergence or C is still responsible for the organization. Stronger mesoscale circulation and more positive mesoscale moisture convergence in the moist areas enlarge the cloud plumes. Deeper and larger flowers produce heavier precipitation, resulting in stronger cold pools which can modify the vertical profiles of C. For this particular case, there is near-surface mesoscale moisture divergence on a scale larger than the cold pools, leading to a net moisture loss from the atmospheric column and weakening the organization at that scale. The flowers become smaller but do not dissipate completely as there is still net moisture convergence on a smaller scale. This serves as an example of how strong cold pools may be detrimental to the self organization process of convective clouds. Further studies examining the interactions of shallow convection and cold pools in an environment with different surface wind speed would enhance the understanding of this process.

A 12-hr shift in the diel cycle not only changes the cloud amount and the rate of cloud organization, but also modifies the interactions between shallow convection and cold pools. After examining how the S2F transition responds to a complete absence of shortwave radiation, the rest of this paper will examine the S2F transition when the shortwave radiation is partially reduced and the longwave radiation is modified because of mineral dust above the clouds.

5. The Radiative Impacts of Mineral Dust on the S2F Transition

Mineral dust was present above the cloud layer when the sugar-to-flower transition took place on February 2–3, 2020. This part focuses on the impacts of mineral dust above the cloud layer on the transition from sugar to flowers through radiation. An additional simulation is performed. In the Dust simulation, a mineral-dust layer is initialized at the beginning with a concentration of 1,600 mg^{-1} between 4 and 5.5 km. The differences in radiation caused by the mineral-dust layer are shown in Figures 8a and 8b, which presents the time series of the domain-mean net shortwave and longwave radiation at the surface (SWNS and LWNS, respectively) of the Control and Dust simulations. The mineral-dust layer reduces the net shortwave radiation at the surface during the day, with a maximum of 65 W m^{-2} around noon local time. The mineral dust also reduces the net longwave radiation at the surface by 1.7 W m^{-2} on average throughout the simulation.

5.1. Free-Tropospheric Mineral Dust and the Transition From Sugar to Flower Shallow Cumuli

The rest of Figure 8 shows the time series of the cloud and rain amounts. The vertical structures and the differences of the cloud and rain water are shown in Figure 9. Since the only difference between these two simulations is the presence of mineral dust above the cloud, and the elevated moisture layer is kept identical, the PW remains the same in both simulations (not shown). It should also be noted that elevated layers of mineral dust tend to be accompanied by elevated moist layers, which reduce the cloud amount because of the enhanced reemission of longwave radiation to the surface (Gutleben, Groß, & Wirth, 2019; Yamaguchi et al., 2015). However, the differences between the Control and Dust simulations stem from the elevated mineral-dust layer only. So the results from these simulations should not be directly compared with observational studies or simulations that compare the cloud system under the absence of both the elevated moisture and mineral dust, such as in Gutleben, Groß, and Wirth (2019). Up until hour 14 (local noon), both simulations produce similar amounts of the cloud water paths (CWP) and cloud fraction (CLD). The Dust simulation then produces slightly more cloud water and cloud fraction than the Control simulation in the afternoon (hours 14–18). The Control simulation catches up and produces more cloud water and higher cloud fraction after sunset (Figures 8c, 8d, and 9c). There is a marginal difference in rain water path and surface precipitation; in general, the Dust simulation produces less rain than the Control as the rain occurs at night when the Dust simulation produces slightly less cloud. Further discussion is deferred to Section 5.2.

When considering the spatial distribution of the clouds (Figures 3 and 10), there are noticeable differences in the patterns and the rates of cloud organization between the Control and Dust simulations. Particularly, there are more flower clouds in the Dust simulation between 16 and 22 hr (14:00 and 20:00 local time), and those flower aggregates are larger. Section 5.3 will show that this arises from differences in the mesoscale circulation that helps accelerate the transition from sugar to flowers in the non-precipitating shallow cumulus regime.
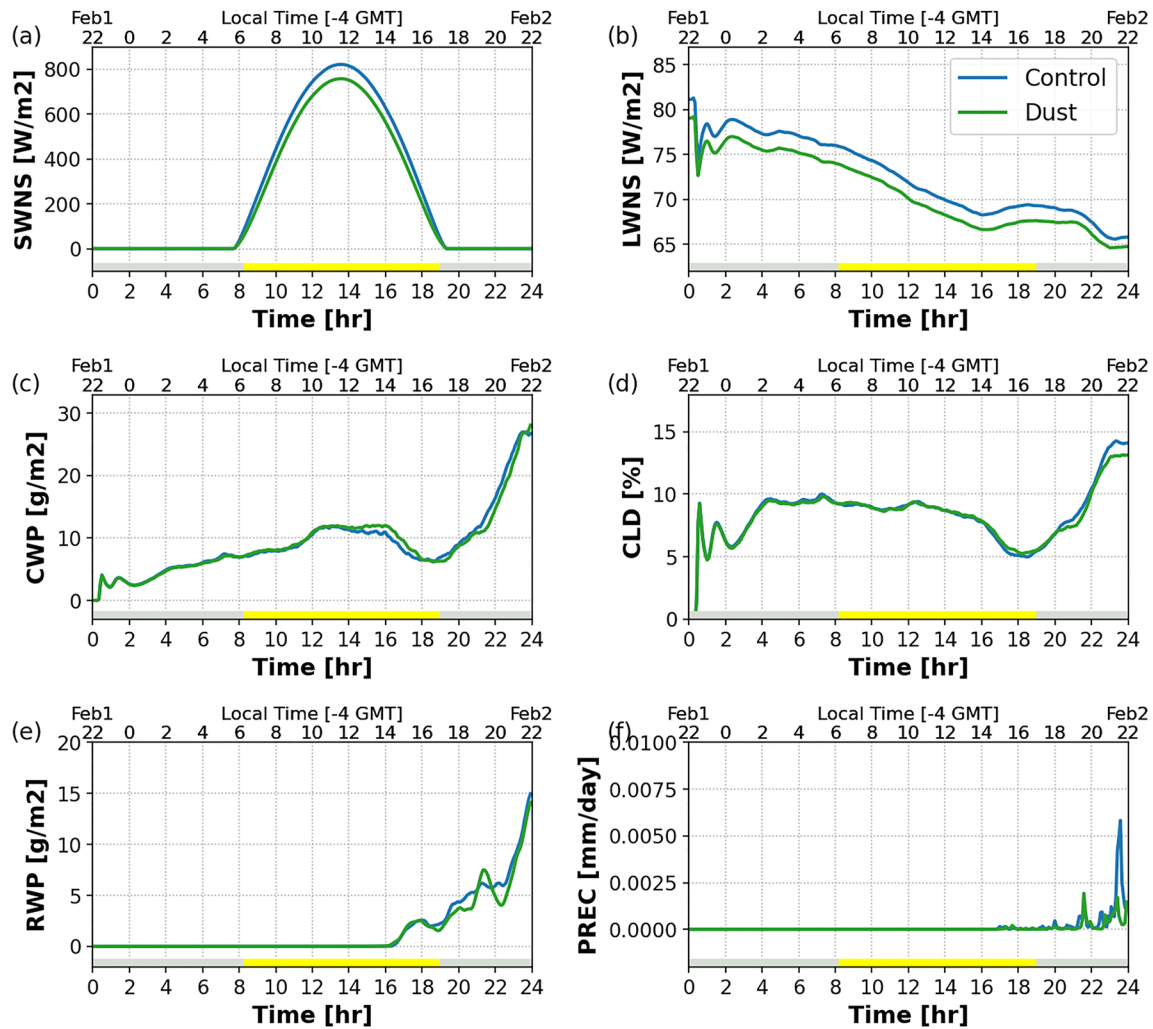
Figure 8. Domain-mean time series of various variables from the Control simulation (without mineral dust, blue) and the Dust simulation (with mineral dust in the free troposphere, green): (a) net surface shortwave radiative flux, (b) net surface longwave radiative flux, (c) cloud water path, (d) cloud fraction, (e) rain water path, and (f) surface precipitation. The bottom *x*-axes indicate time after the simulations begin, while the top *x*-axes indicate the local time of both simulations (same local time for both). The gray and yellow bands represent the day and night, respectively, shown at the bottom of each panel.

5.2. Large-Scale Impacts of the Mineral Dust

Figure 11 shows the radiative heating properties of the mineral dust and their effects on the cloud production, which in turn affects the boundary layer heating rate and the cloud system development. At night (hours 0–8), the elevated mineral-dust layer increases longwave warming in the cloud layer (Figure 11b), resulting in anomalous warming and weaker buoyant turbulence kinetic energy (TKE) production near the cloud top (Figures 11d and 11e). This stabilizes the cloud layer and results in less cloud condensate (Figure 9c); these initial differences are small and barely noticeable in the CWP and CLD time series (Figures 8c and 8d). During the day (hours 8–18), the elevated mineral-dust layer absorbs shortwave radiation, resulting in less shortwave heating beneath (Figure 11a). Since the Dust simulation has less cloud at night, in the absence of dust radiative effects, the system would have experienced less cloud-top longwave cooling during the day. However, the shortwave absorption by mineral dust cools the cloud top, destabilizing the cloud layer and driving stronger near-inversion buoyant TKE production in the Dust simulation (Figures 11d and 11e), resulting in more clouds (Figures 8c, 8d, and 9c). After sunset (hours 18–24), the additional longwave heating due to mineral dust dominates again, suppressing the cloud-top buoyant TKE production (Figure 11f) and upward water flux, hence reducing the amount of cloud and precipitation.
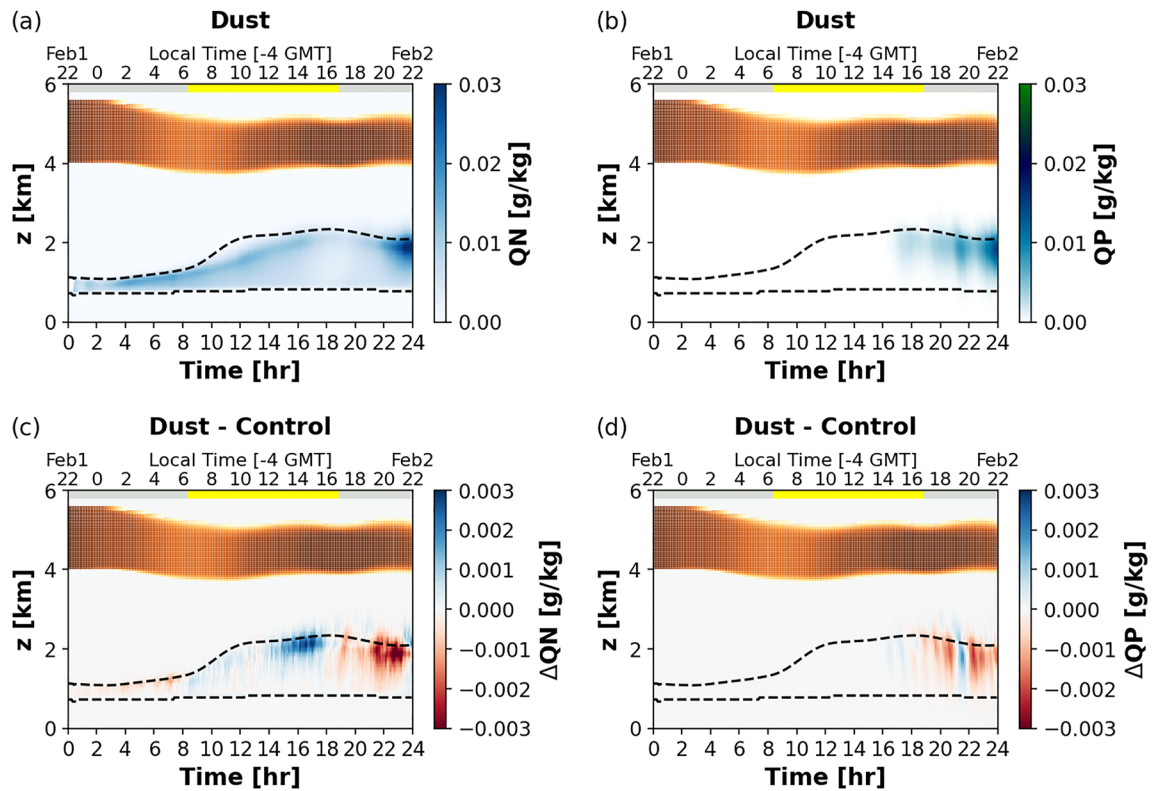
Figure 9. Domain-mean time series of (a, b) cloud and rain water mixing ratios (QN and QP, respectively) from the Dust simulation. (c, d) Differences in QN and QP between the Dust and Control simulations. The black dashed lines indicate the cloud top and base heights of the Dust simulation. The brown shading indicates the mineral-dust layer. The bottom x-axes indicate the time after the simulations begin and the top x-axes indicate the local time of the simulations, as in Figure 2.

The mineral dust remains mostly in the free troposphere throughout the simulation. Only a small concentration (on the order of 0.001 mg^{-1}) is entrained into the cloud layer. So the majority of the effect of mineral dust is from above the clouds. The difference in radiative heating rate between the Control and Dust simulations is felt after sunrise, as the shortwave effect of the dust is much stronger than other contributors to shortwave heating. When the clouds aggregate during the day, the local radiative heating rates (inside and outside of the clouds) start to diverge between these two simulations. This is explored in the following section.

5.3. Local Impacts of the Mineral Dust

The rest of this section aims to understand the radiative impact of the mineral dust on the mesoscale organization of the clouds from the local perspective. Figure 12 shows a cross section through two flower aggregates from the Dust simulation at hour 16 of the simulation (18 UTC or 14:00 local time), when the solar radiation is still strong. Figure 12b shows the cross section of specific humidity (QV, colors) and the cloud condensate of 0.1 g kg^{-1} or greater (QN, contours). By this time, a small amount of mineral dust (less than 0.001 mg^{-1}) is entrained into the cloud plumes; the precipitating downdrafts at later hours further assist in bringing the mineral dust to the surface (not shown). Because the concentration is so small, the radiative heating rate of the dust inside the clouds is negligible compared to that of the cloud liquid water.

The mineral dust in the free troposphere results in extra cloud-top shortwave cooling and longwave heating (Figures 12c and 12d), but they are much weaker compared to the cloud-top shortwave heating and longwave cooling due to the water vapor and liquid water inside the cloud layer (Figures 12e and 12f). The net radiative heating rate (all atmosphere) from the same time is shown in (Figure 13b). There is net radiative cooling at the cloud tops and net radiative heating inside the cloud plumes. The net radiative heating rate perturbations binned by the TWP quartiles (RAD'') of both simulations at hour 16 are shown in Figure 14a. Not only is there more cloud-top net radiative cooling in the moistest TWP quartile (Q4 or the cloudy regions) of the Dust simulation but there is also more sub-cloud-layer cooling in the driest TWP quartile (Q1 or the cloud-free regions). It
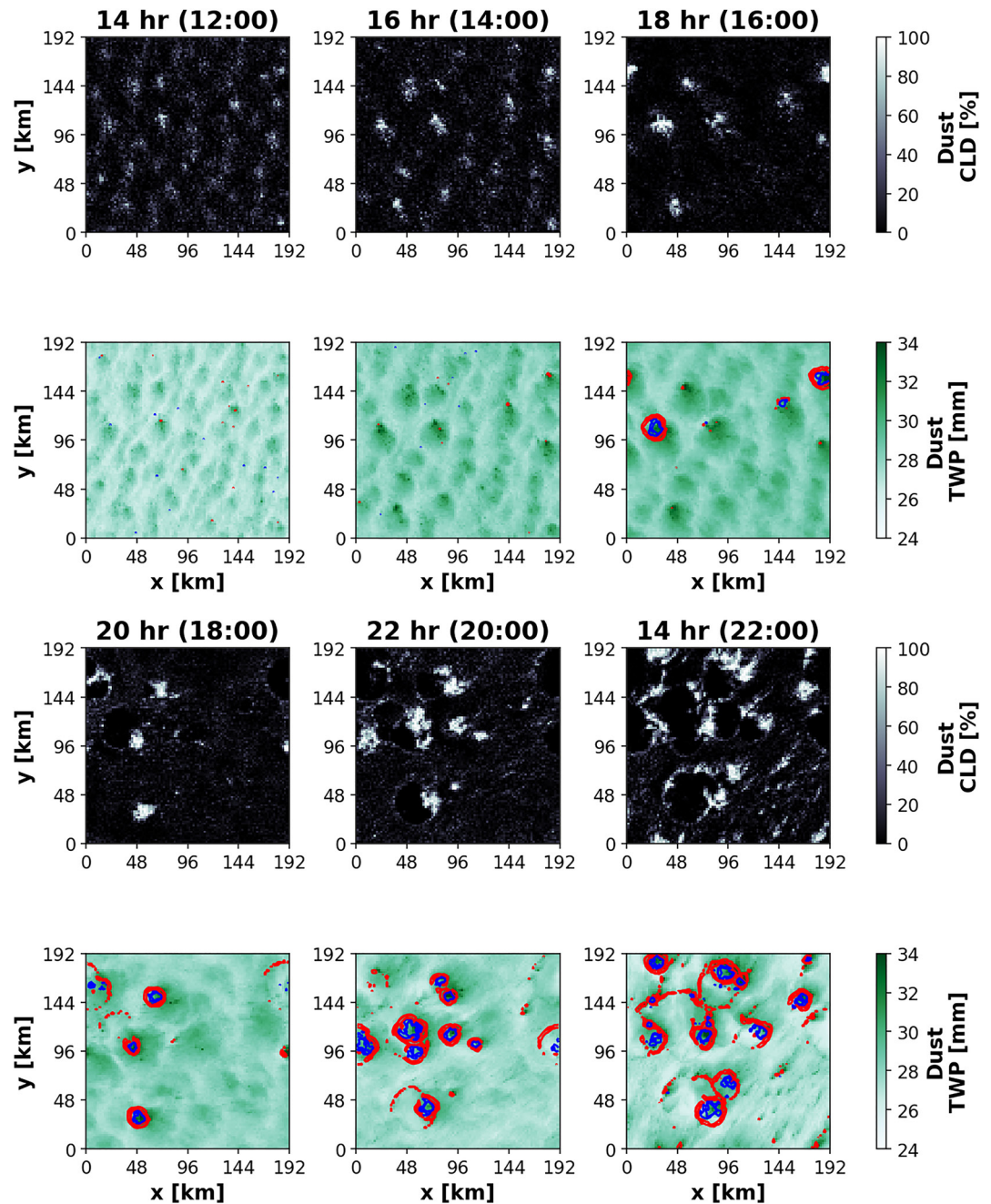
Figure 10. As in Figure 3 but for the Dust simulation. The local time of the Dust simulation is the same as the Control simulation. There are more cold pools relative to Figure 3.

will be shown that the greater horizontal heating contrast can drive stronger mesoscale circulation and cloud organization.

Figure 13 further shows the net radiative heating rate at hour 14 (12:00 p.m., left) and hour 18 (16:00 p.m., right). The insolation becomes weaker as the simulation approaches sunset. Therefore, at 16:00 p.m., which is less than 1 hr before the insolation becomes zero, the longwave cooling effect of water vapor and liquid water dominates. This is consistent with Figures 14b and 14c which shows stronger cloud-top cooling in the moist and cloudy areas (Q4) when the organization is stronger.
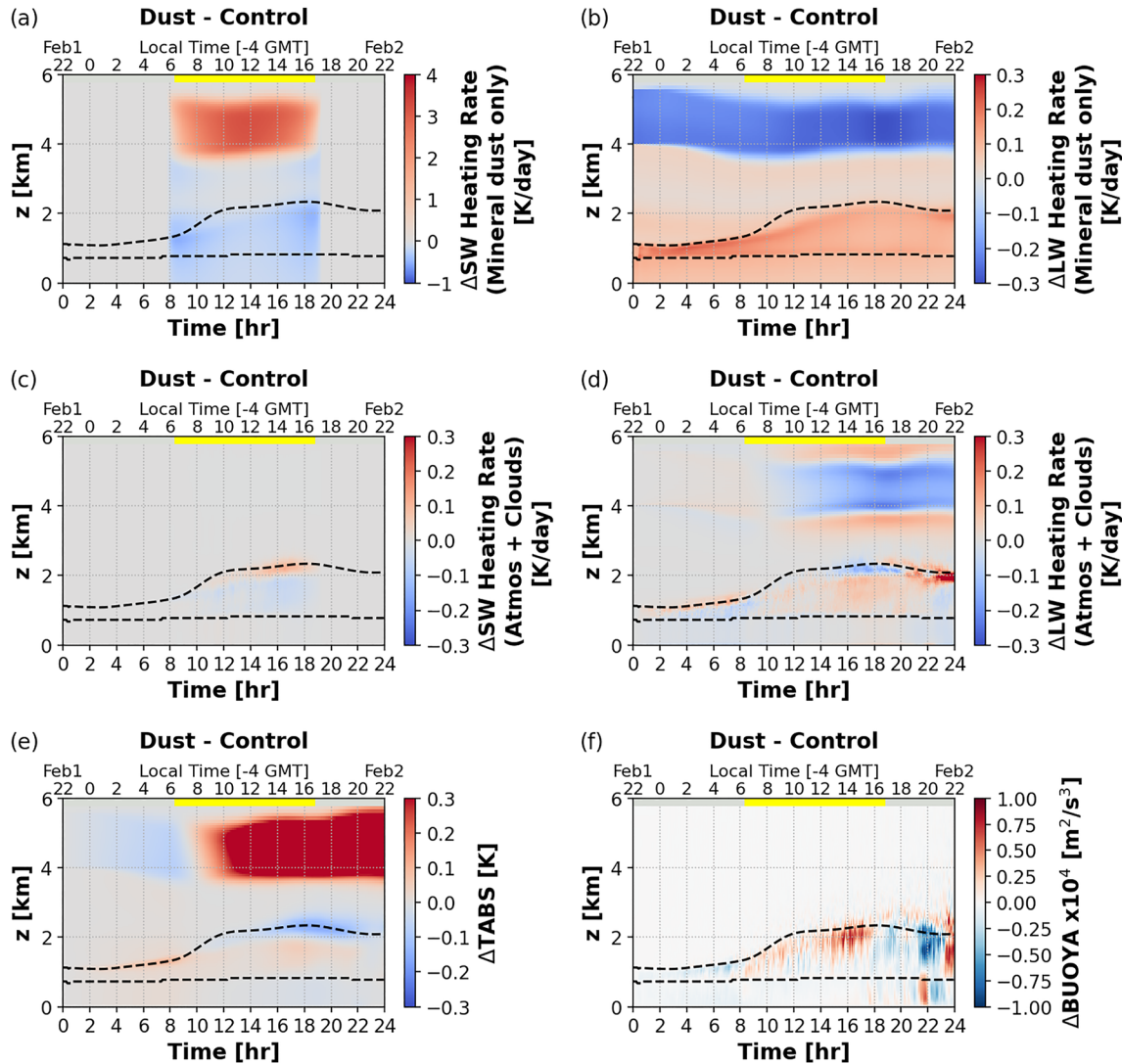
Figure 11. Time-height curtains of the differences between the Dust and Control simulations: (a, b) shortwave and longwave radiative heating of the mineral dust (by definition, they are zero in the Control simulation), (c, d) the shortwave and longwave radiative heating rate from the atmosphere excluding the radiative impacts of the mineral dust, (e) the atmospheric temperature, and (f) the resolved and subgrid-scale buoyant turbulence kinetic energy production (or buoyancy flux).

That the air inside flower clouds is cooler than the surrounding regions is true at all times and consistent in both simulations. Figure 14d shows the temperature perturbations (T'') binned by the TWP quartiles. At later times, when the flower clusters are larger, the cooling anomaly in the moistest TWP quartile (T'' from Q4) is almost -1 K in the Dust simulation (Figure 14e) because of more longwave cooling from more water vapor and liquid water. During the times when the Dust simulation produces more clouds than Control, T'' from Q4 of the Dust simulation is also more negative (Figure 14f, until hour 18). This implies that a rising air parcel inside the clouds from the Dust simulation will gain more buoyancy as it encounters the cooler air. This condition is consistent with stronger upward vertical velocity anomaly inside the cloud plumes (w'', Figures 14g–14i) leading to stronger lower-level moisture convergence (positive C, Figures 14j–14l) in the moist regions. The w'' and C profiles are more positive in Q4 of the Dust simulation during the times when the Dust simulation produces more clouds (Figures 14i and 14l).

The differences in RAD'', T'', w'', and C between the Dust and Control simulations hinder mesoscale organization in Dust at night (hours 18–22 in the right column of Figure 14). During this time, the extra longwave heating due to greater cloud liquid water in the Dust simulation helps to stabilize the cloud layer and reduce the horizontal heating contrast, thus weakening the mesoscale vertical velocity perturbations (less positive w'' in Q4) and the
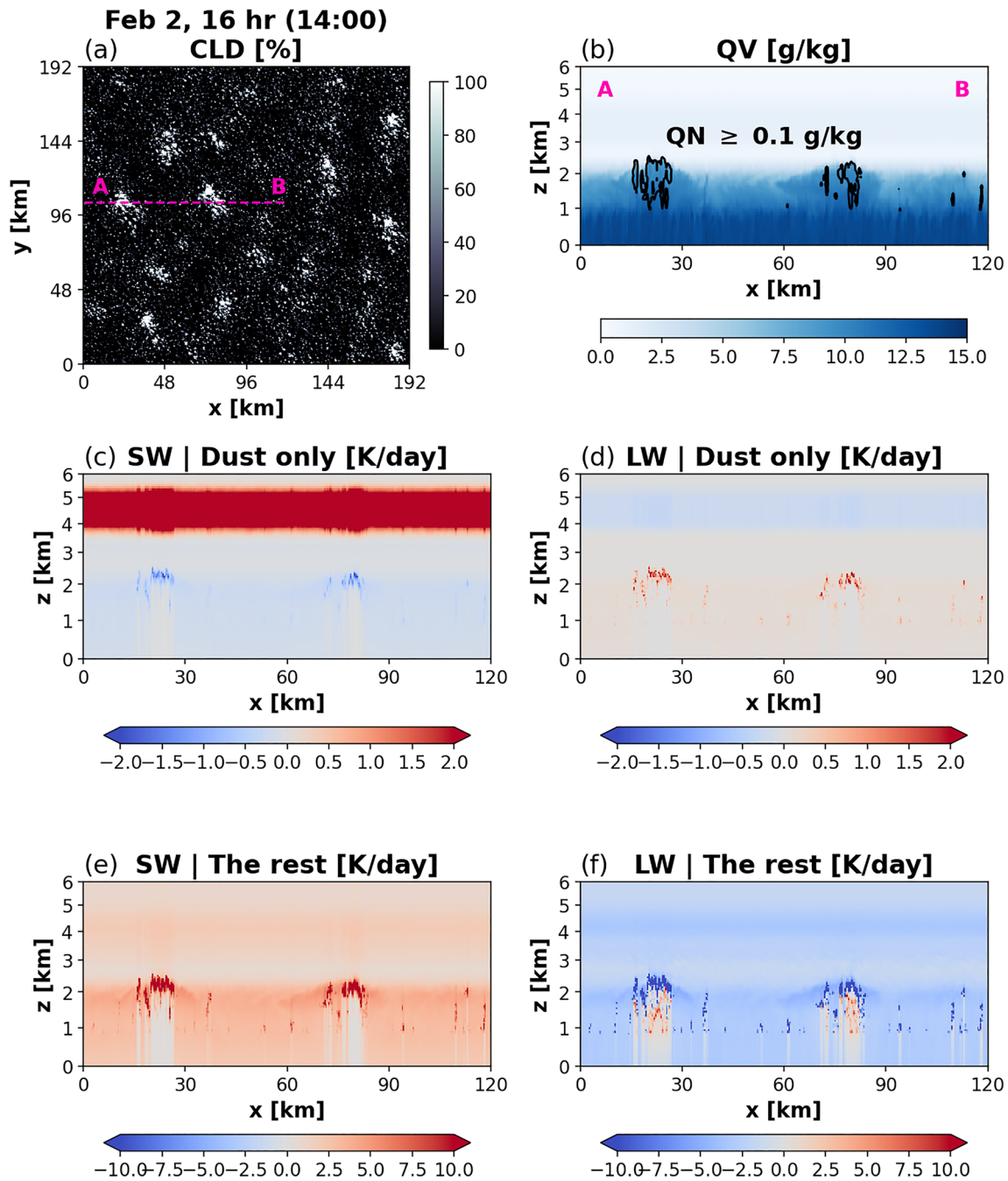
Figure 12. (a) A snapshot of the cloud fraction from the Dust simulation at hour 16 (14:00 local time or 18 UTC), when the clouds are aggregating. A cross section is drawn following the dashed pink line through two aggregating "flower" shallow cumuli. (b) Cross sections of the specific humidity (QV, colors) and the cloud condensates (QN, contours) of 0.1 g kg⁻¹ or greater. (c, d) Cross sections of shortwave and longwave radiative heating rates from only the mineral dust. (e, f) Shortwave and longwave radiative heating rates from everything else except for the mineral dust.

mesoscale convergence of total water to the moist areas (less positive C). Therefore, the mesoscale organization is weaker and there is less cloud condensate in the Dust simulation than Control after sunset. At hour 24, the mesoscale circulation in the Dust simulation is strengthened again. At this point, more mineral dust is entrained into the boundary layer but it is not removed by sedimentation in the simulation since it is only allowed to interact with the radiation scheme. An accurate representation of this state requires coupling the mineral dust with the cloud microphysics scheme and is beyond the scope of this paper, which focuses on the aerosol-radiation interaction and its impacts on the clouds.
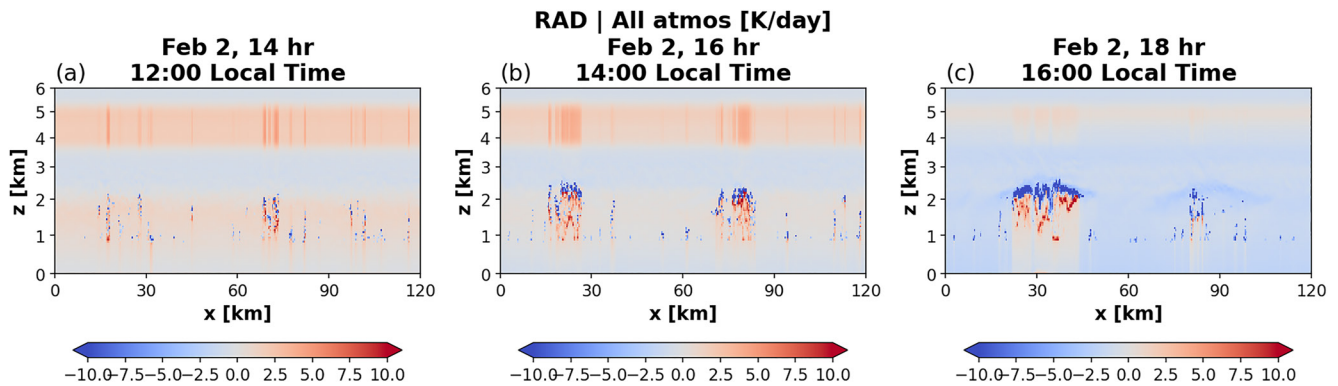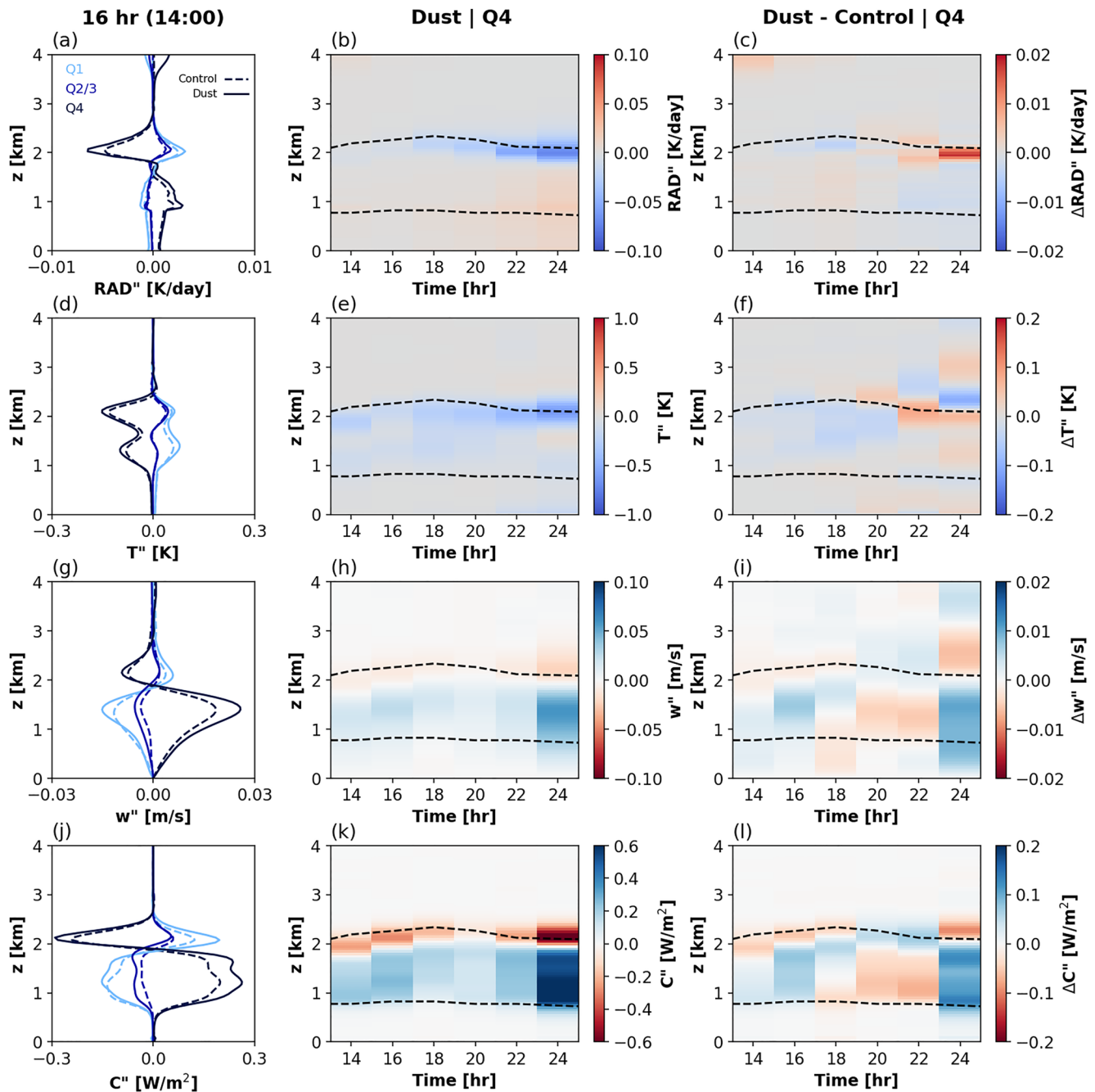
Figure 13. Snapshots of the net radiative heating (all atmosphere) from the Dust simulation at (a) 12:00 local time, (b) 14:00 local time, which is the same as in Figure 14, and (c) 16:00 local time, which is within 1 hr before sunset.

Figure 15 summarizes the above findings by presenting time series of two organization diagnostics, and the ratios of the buoyant TKE production and total water spectra between Dust and Control. They consistently show that the Dust simulation has stronger organization rate during the end of the day (larger mean area of cloud aggregates and greater normalized TWP standard deviation, Figures 15a and 15b). The cloud-layer TKE production spectra and the boundary-layer QT spectra in the mesoscale of the Dust simulation increase with the organization diagnostics (Figures 15c and 15d). The TKE production and QT spectral ratios between the Dust and Control simulations associated with wavelengths greater than 4 km and smaller than 48 km are greater than 1 between hours 8 and 20 (Figures 13e and 13f). They suggest that during this period, there is stronger TKE production inside the cloud layer and the boundary-layer total water (vapor, cloud water, and rain) is also more aggregated in the mesoscale in the Dust than Control simulations. Based on this analysis alone, it is impossible to deduce whether the stronger TKE production drives the QT aggregation, or vice versa. However, a previous study that examines a self-organization mechanism of the flower clouds has shown that the QT aggregation responds to the buoyant TKE production changes (Narenpitak et al., 2021). The time lag is apparent in their study as the self-organization strength between the two simulations differed more strongly.

5.4. Discussion

In the second part, the radiative impacts of mineral dust in the free troposphere on the cloud organization has been explored. In general, mineral dust can modify the mesoscale circulation associated with the flower clouds via two pathways: a direct response and a delayed response. If a large concentration of mineral dust is entrained into the cloud layer, for example, and is redistributed unevenly between the cloud plumes and away from the clouds, the mineral dust can directly change the local radiative heating rates, stability of the atmosphere, and the mesoscale circulation. This process describes a direct response. By design, a direct response does not take place in the simulations presented in this paper. This study describes the second pathway, the delayed response to the mineral dust. Over the course of 24 hr, the presence of the mineral dust modifies the cloud amount, which later dominates in modifying the local radiative heating rates. This further affects the cloud amount and cloud aggregation, which positively correlates with the mesoscale circulation strength. Overall, this is an example of how the free-tropospheric mineral dust modifies the cloud amount and the mesoscale circulation through the interactions of aerosol, clouds, and radiation.

This study focuses only on the role of mineral dust in the EML on radiation, and how that interacts with the clouds. Although including a mineral-dust layer does not change the cloud amount as much, the presence of the extra humidity in the EML and its effect on the radiation and the boundary layer cloud is non-negligible. A previous study, Yamaguchi et al. (2015), examined the effects of elevated moisture and smoke layers on shallow clouds, particularly the stratocumulus to cumulus transition in the North East Pacific. They found that an EML weakens the cloud-top radiative longwave cooling, increases the daytime cloud evaporation, and thus reduces the cloud water path and cloud depth. It is hypothesized that an EML would similarly weaken the cloud-top radiative cooling of the flower clouds and might even slow down the transition from sugar to flowers. So a simulation that removes both the EML and the elevated dust layer would also produce more clouds than a simulation with both,

Figure 14. (a) Vertical profiles of the mesoscale net radiative heating perturbations (RAD'') at 18 UTC (hour 16 or 14:00 local time, same as in Figure 12) binned by total water path (TWP) quartiles. (b) Time-height curtains of RAD'' averaged over the highest TWP quartile or Q4 from the Dust simulation at 16 UTC to 2 UTC (hours 14 through 24). (c) Time-height curtains of the differences in RAD'' of Q4 between the Dust and Control simulations at hours 14 through 24. (d–f) As in Panels (a–c) but for the mesoscale temperature perturbations (T''). (g–i) As in Panels (a–c) but for the mesoscale vertical velocity perturbations (w''). j–l As in Panels (a–c) but for the mesoscale convergence of total water (C).
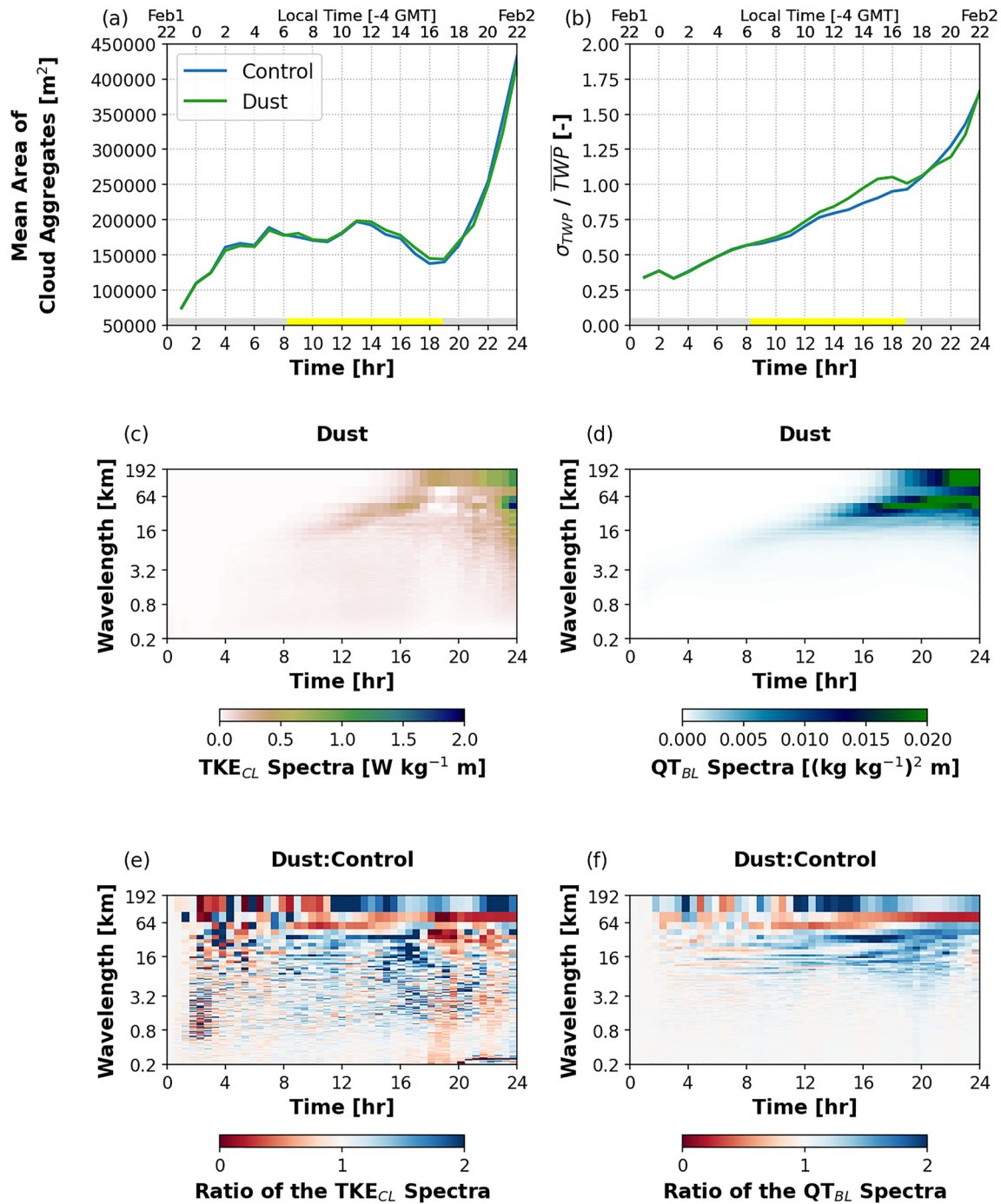
Figure 15. Organization diagnostics from the Control and Dust simulations: (a) the mean area of cloud aggregates and (b) the normalized total water path standard deviation. (c) The hourly spectra of the cloud-layer buoyant turbulence kinetic energy (TKE_{CL}) production from the Dust simulation. (d) The hourly spectra of the boundary-layer total water mixing ratio (QT_{BL}) from the Dust simulation. (e) Ratios of the TKE_{CL} spectra between the Dust and Control simulations. (f) Ratios of the QT_{BL} spectra between the Dust and Control simulations.

which would be consistent with Gutleben, Groß, and Wirth (2019). A follow on study to test this hypothesis is recommended.

6. Conclusions

The ATOMIC and EUREC⁴A field campaigns took place in January–February 2020 over the Atlantic Ocean east of Barbados. One of the goals is to advance the understanding of shallow cumulus clouds, mesoscale processes, circulation, and their interactions with the weather and climate. On 2 February 2020, a shallow cumulus transition from sugar to flower clouds was observed. The event was simulated using a Lagrangian LES following an airmass trajectory along the tradewind for 24 hr. The cloud depth and cloud liquid water increase along the trajectory with large-scale upward vertical motion. As the transition from the sugar cloud state to the flower cloud state takes place, cloud aggregation and mesoscale organization become stronger, despite weakening surface wind speed. Net convergence of moisture associated with mesoscale circulation renders the moist areas moister, strengthening the organization and supporting the cloud transition.

The observed sugar-to-flower transition occurred during the day and produced light precipitation and cold pools at night. However, if the diel cycle is shifted such that the transition takes place at night, the clouds deepen more rapidly and organize more strongly. In other words, the shortwave radiation introduced to shallow cumuli at the time of the sugar-to-flower transition slows down the process because of extra heating and stabilization, which weakens the mesoscale circulation and the moisture convergence.

When the transition takes place in a complete absence of shortwave radiation, the cloud layer deepens more. Deeper flower clouds lead to more precipitation and stronger cold pools, which initiate new convection through dynamical lift at the cold pool edges. Each cloud and cold pool interaction cycle lasts a few hours, and there are a few cycles of such interactions throughout the night. Strong cold pools are detrimental to the organization process if they lead to a net moisture divergence in the moist and cloudy areas. Since there is a tight connection between surface wind speed, surface fluxes, and the cold pool strength, further studies should incorporate changes in the surface wind speed, which also exhibit a diel cycle in the tradewind regime, and examine how they influence the properties of the cold pools.

During the field campaigns, the observed sugar-to-flower transition occurred under a layer of mineral dust in the free troposphere. The mineral dust is accompanied by an elevated layer of moisture, which by itself reduces the cloud amount because of the reemission of longwave radiation (Yamaguchi et al., 2015). The elevated mineral-dust layer dims the shortwave radiation, and also increases the longwave reemission slightly. When isolating the effects of the free-tropospheric mineral dust from the elevated moisture layer, it is found that mineral dust above the sugar-to-flower transition slightly increases the cloud amount and strengthens the cloud organization during the day due to shortwave cooling, but has the opposite effect at night because of the extra longwave heating. Future studies should explore further how the absence of both the elevated mineral dust and moisture layers affect the cloud system.

Overall, both the diel cycle and the free-tropospheric mineral dust have impacts on the radiation, but the 12-hr delay in the diel cycle has a much stronger radiative effects than the mineral dust. The diel cycle shift completely alters the timing of the atmospheric heating by the shortwave radiation and the timing of the boundary-layer destabilization. The daytime destabilization is common in shallow cumulus fields and is known to dissipate the clouds (Vial et al., 2019). This explains why most shallow cumuli are thicker at night and why flower clouds are observed mostly at night during field campaigns (Pincus et al., 2021; Stevens et al., 2021; Vial et al., 2021). The free-tropospheric mineral dust, while modifying both the shortwave and longwave radiation, has less impact on the cloud system if only the radiative effect is considered. In reality, the dust particles could also act as cloud condensation nuclei that might lead to a stronger buildup of liquid water and stronger drizzle. These may alter the cloud and cold pool interaction further. Additional simulations that allow the mineral dust to interact with both the radiative and cloud microphysics schemes will shed light on this. The sensitivity of the sugar-to-flower transition to atmospheric radiation raises the interesting question of its response to anthropogenic climate change, which involves a warmer ocean, atmosphere, and higher greenhouse gas concentrations, all of which change atmospheric radiation. This warrants further investigation of the cloud system.

Appendix A: The Surface Fluxes From the Control and Diel+12h Simulations

Previous studies found that at night, shallow cumulus clouds have greater cloud fraction and are deeper than during the day. Often, they have stronger surface wind speed at night, leading to stronger latent heat flux (LHF), deeper cloud layer, stronger mixing, and weaker sensible heat flux (SHF), which can promote the cloud formation further (Nuijens & Stevens, 2012; Vial et al., 2021). In this case, the surface wind speed are the same between Control and Diel+12h simulations. In both simulations, the LHF and SHF tendencies follow that of the surface wind speed (Figure A1). The Diel+12h simulation has weaker LHF and SHF than the Control simulation during the first 12 hr. This is as expected, because it is daytime in the first 5 hours of the Diel+12h simulation; the shortwave heating warms the boundary layer and the SHF does not need to be as strong. The LHF is initially smaller as the Diel+12h simulation initially produces less cloud water than the Control simulation. In the second half, the Diel+12h simulation produces stronger LHF and SHF than Control, and hence stronger Bowen ratio.
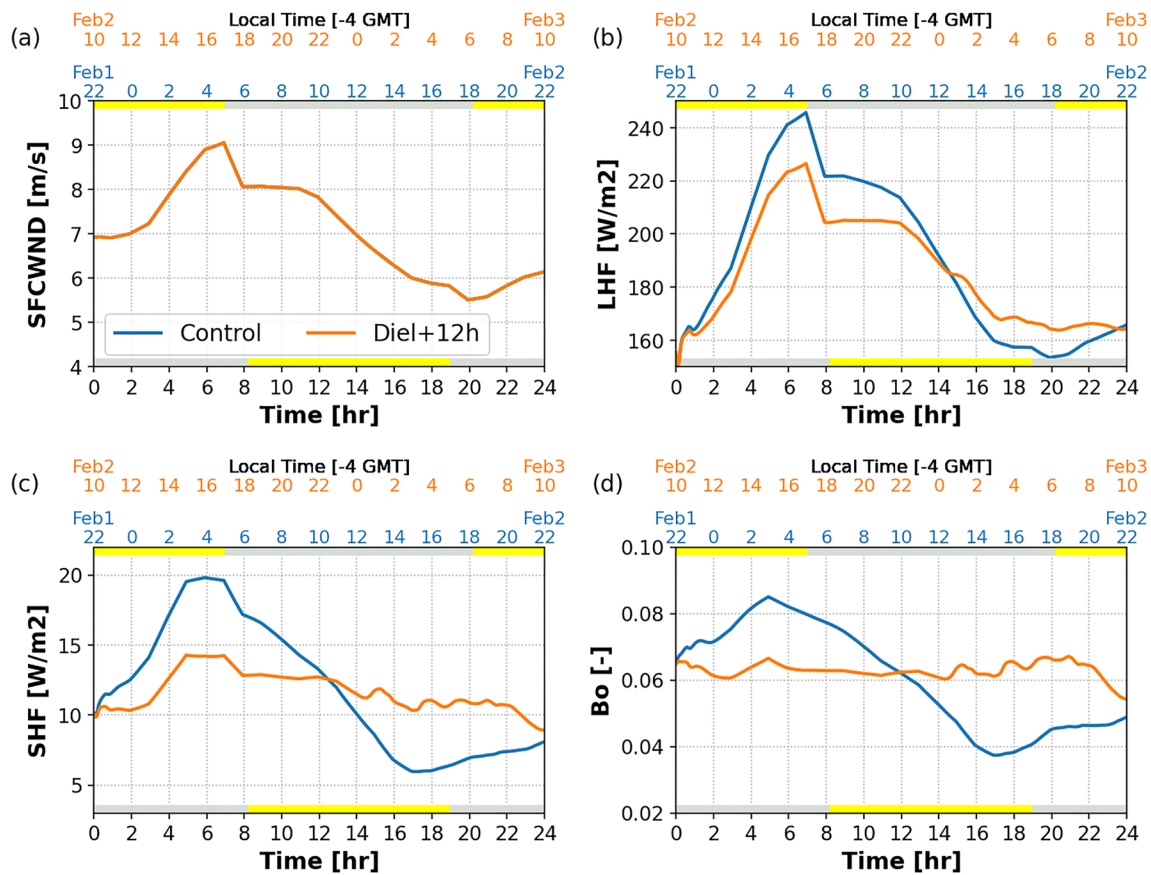
Figure A1. As in Figure 1 but for (a) the surface wind speed, (b) the surface latent heat flux (LHF), (c) surface sensible heat flux (SHF), and (d) the Bowen ratio (Bo = SHF/LHF) from the Control and Diel+12h simulations.

Appendix B: The Total Water Perturbation Budget

The budget of mesoscale total water perturbations $\left(q_t''(x_m, y_m, z, t)\right)$ can be described as:

$$\frac{\partial q_t''}{\partial t} = \mathcal{A} + \mathcal{F} + \mathcal{C} + \mathcal{S}. \tag{B1}$$

Each term on the right hand side of Equation B1 is as follows: The first term is the advection of mesoscale variability due to the trajectory-relative large-scale wind $\left(\overline{\boldsymbol{v}}(z,t)\right)$ and the mesoscale perturbations of the wind velocity $(\boldsymbol{v}''(x_m, y_m, z, t))$ in both the horizontal and vertical directions:

$$\mathcal{A} = -\left(\overline{\boldsymbol{v}} + \boldsymbol{v}''\right) \cdot \nabla q_t''. \tag{B2}$$

Let [ ]″ denote coarse-graining of the cumulus-scale field inside the brackets to a mesoscale region of 16×16 km², and let ρ denote the reference density profile. The second term represents the vertical and horizontal gradients of the cumulus-scale q_t flux $\left(\boldsymbol{v}''' q_t'''\right)$ coarse-grained to 16×16 km²:

$$\mathcal{F} = -\frac{1}{\rho} \nabla \cdot \left[\rho \boldsymbol{v}''' q_t'''\right]''. \tag{B3}$$

Equation B3 was derived with the anelastic approximation used in SAM. $\mathcal{F}$ could also be referred to as the total water transport by thermals in cumulus scales.

The third term is the mesoscale vertical advection of large-scale q_t $\left(\overline{q_t}(z,t)\right)$:

$$C = -w'' \frac{\partial \overline{q_t}}{\partial z}. \tag{B4}$$

As described in the main text, because $\frac{\partial \overline{q_t}}{\partial z}$ is always negative in the shallow cumulus layer, the signs of C follow the signs of w'', which imply local convergence and divergence based on the mass continuity equation. Thus, a positive C physically means there is a convergence of the total water into the considered mesoscale tile.

Finally, the fourth term is the source term of q_t'', which represents the mesoscale perturbations of the precipitation mass flux (F_p) divergence:

$$S = -\frac{1}{\rho} \left[\frac{\partial F_p}{\partial z}\right]''. \tag{B5}$$

In a heavily-precipitating shallow cumulus deck, the mesoscale perturbations of the precipitation mass flux divergence or S is nontrivial. A full derivation of the q_t'' budget can be found in Appendix D of Narenpitak et al. (2021).

These four terms from the Control, Diel+12h, and Dust simulations are shown in Figures B1–B3, respectively.
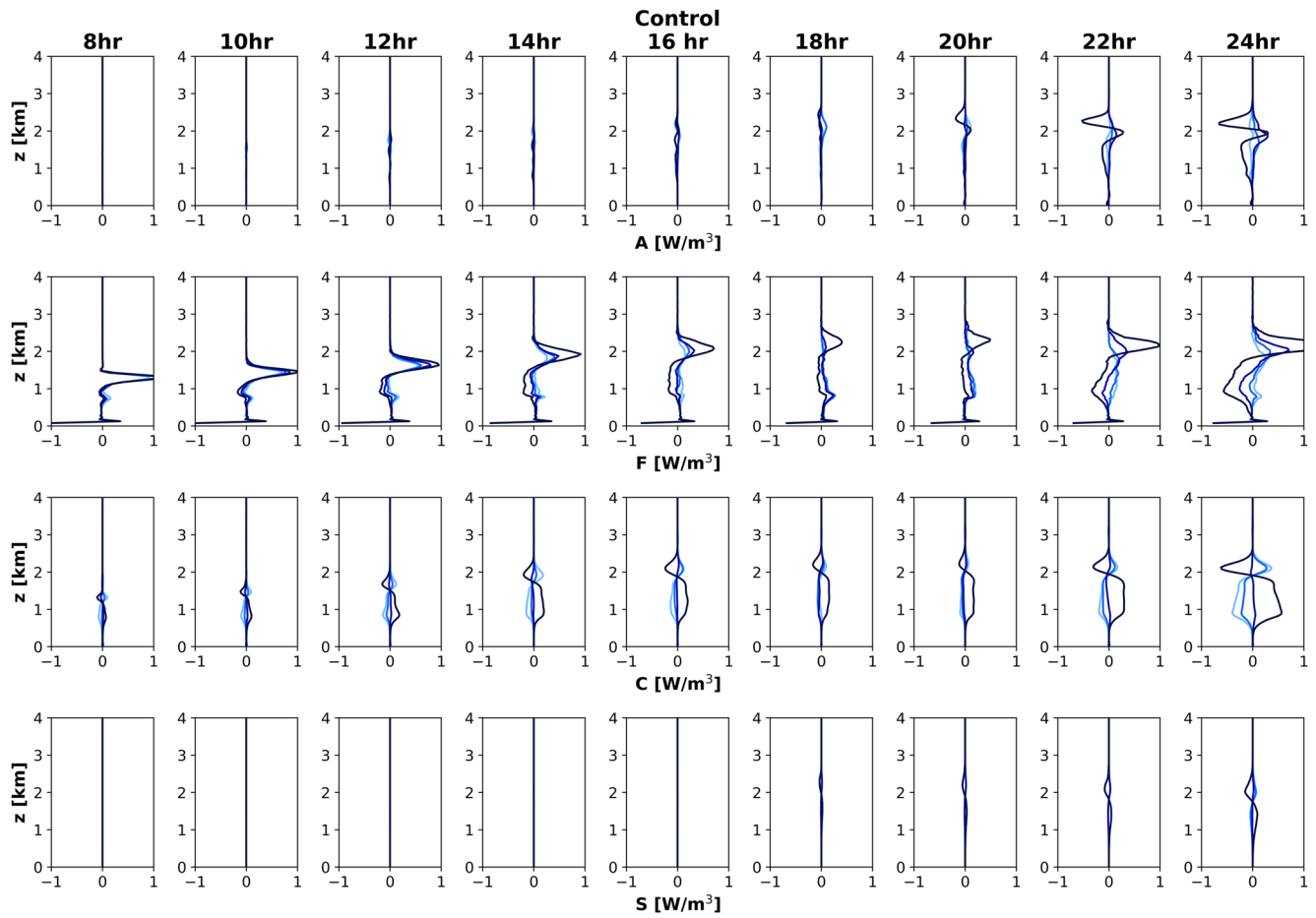
Figure B1. Vertical profiles showing the four main terms in the budget of mesoscale total water perturbations $\left(q_t''\right)$ from the Control simulation: (top row) The advection of mesoscale q_t variability due to the large-scale and mesoscale winds in both the horizontal and vertical directions ($\mathcal{A}$), (second row) the vertical and horizontal gradients of the cumulus-scale q_t flux coarse-grained to a mesoscale tile also in both the horizontal and vertical directions ($\mathcal{F}$), (third row) the mesoscale vertical advection of large-scale q_t or the mesoscale convergence of total water ($\mathcal{C}$), and (bottom row) the mesoscale perturbations of the precipitation mass flux divergence ($\mathcal{S}$). All of these profiles are computed for the 16-km tile size and binned by the total water path quartiles, from Q1 representing the driest regions (light blue) to Q4 representing the moistest regions (dark blue). The profiles are shown every 2 hours from hours 8 (left) to 24 (right).
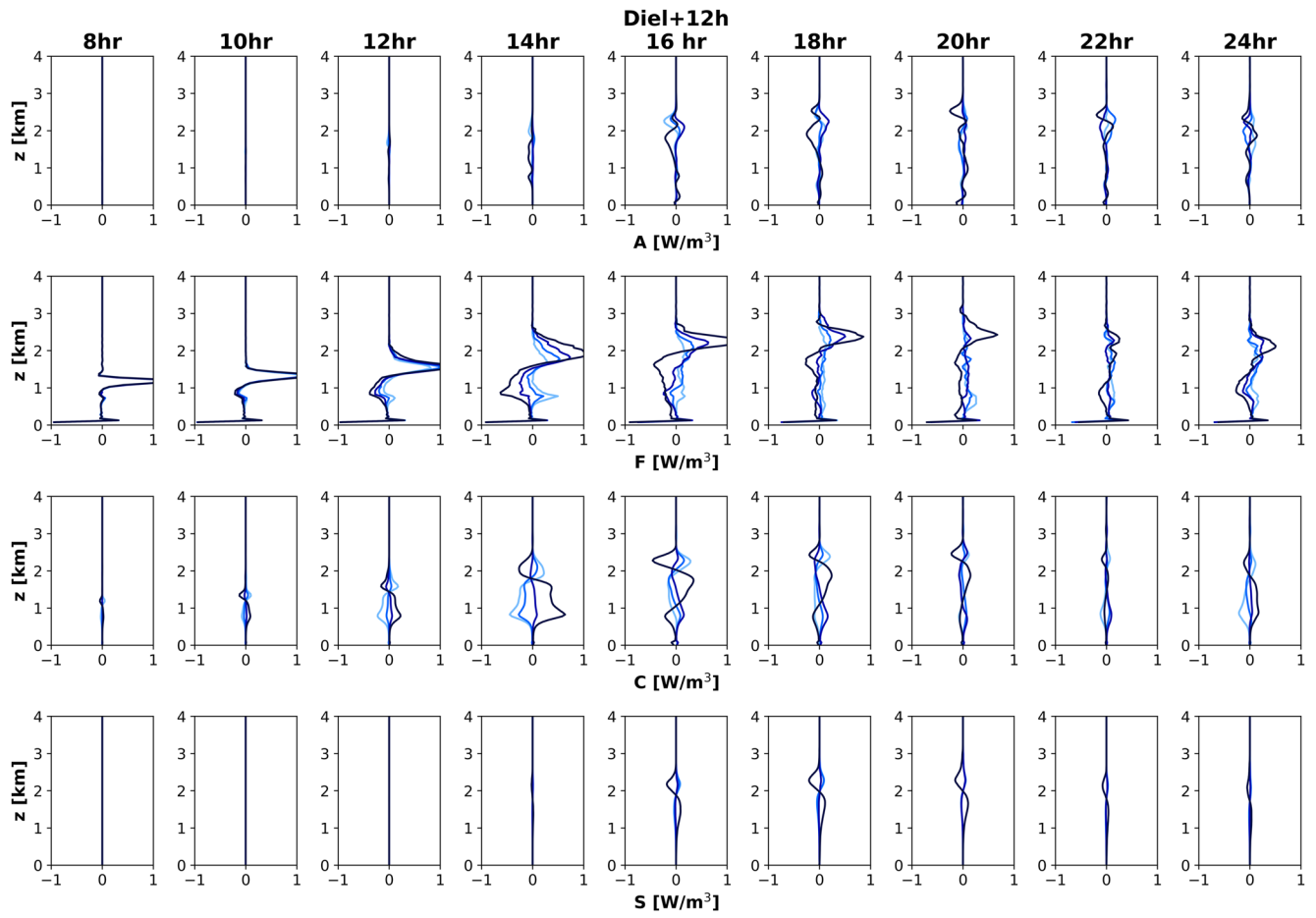
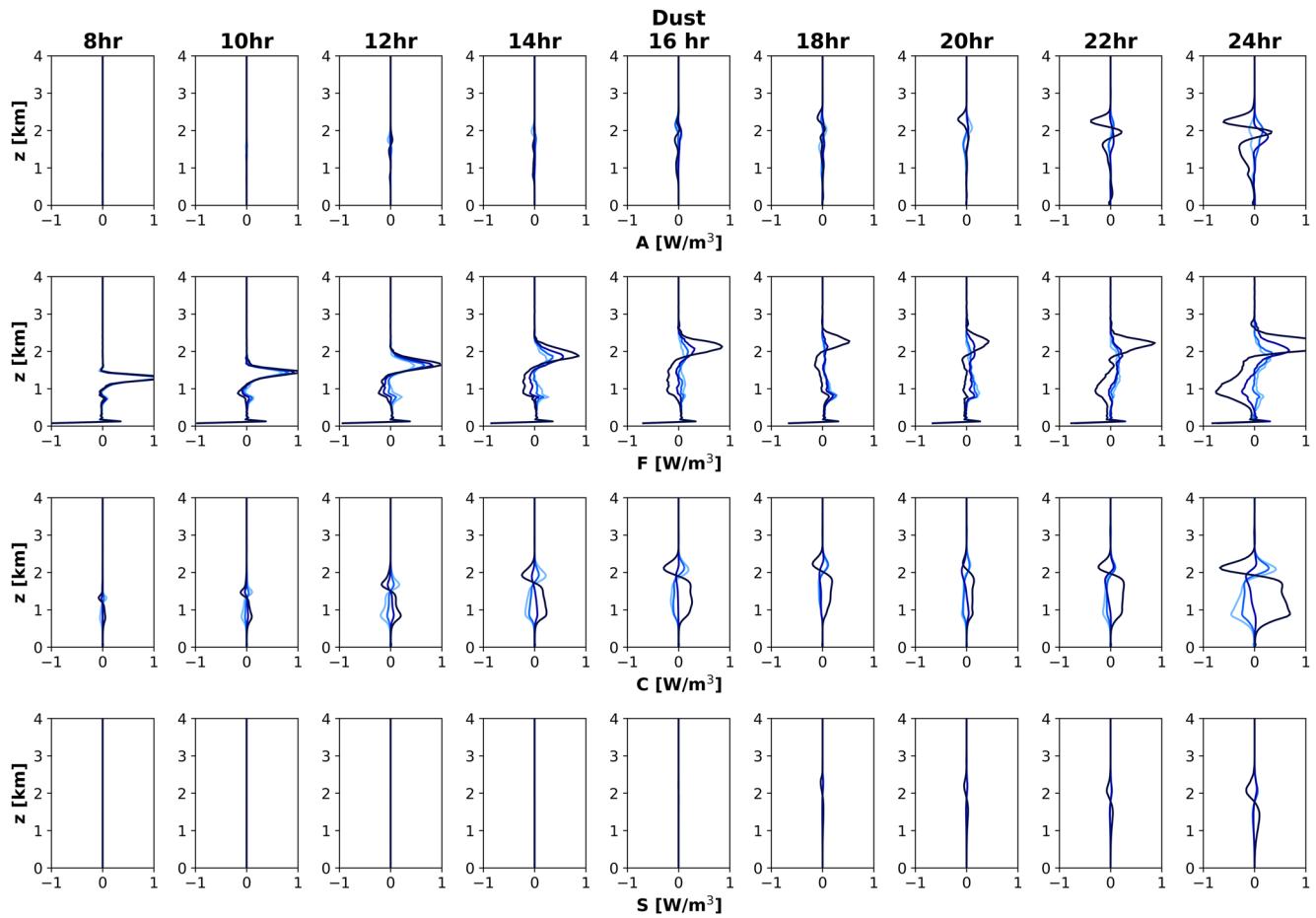**Figure B2.** As in Figure B1 but for the Diel+12h simulation.

Figure B3. As in Figure B1 but for the Dust simulation.

Figure 6 and B2 show that between hours 16 and 20, when the Diel+12h simulation produces a lot of cold pools, the C term is negative in the subcloud layer of the highest TWP quartile (Q4) when using the 16-km mesoscale tile size. Figures B4d–B4f shows that when smaller tile sizes are used (6.4 km or smaller), $C > 0$ everywhere in the cloud layer of Q4, meaning that there is still net moisture convergence in the moist columns associated with the clouds despite the moisture divergence near the surface. The near-surface mesoscale moisture divergence is associated with the gust fronts of the cold pools. Sufficiently high resolution is needed to represent this process. This is demonstrated further in Figure B5 and summarized in Figures B4a–B4c.
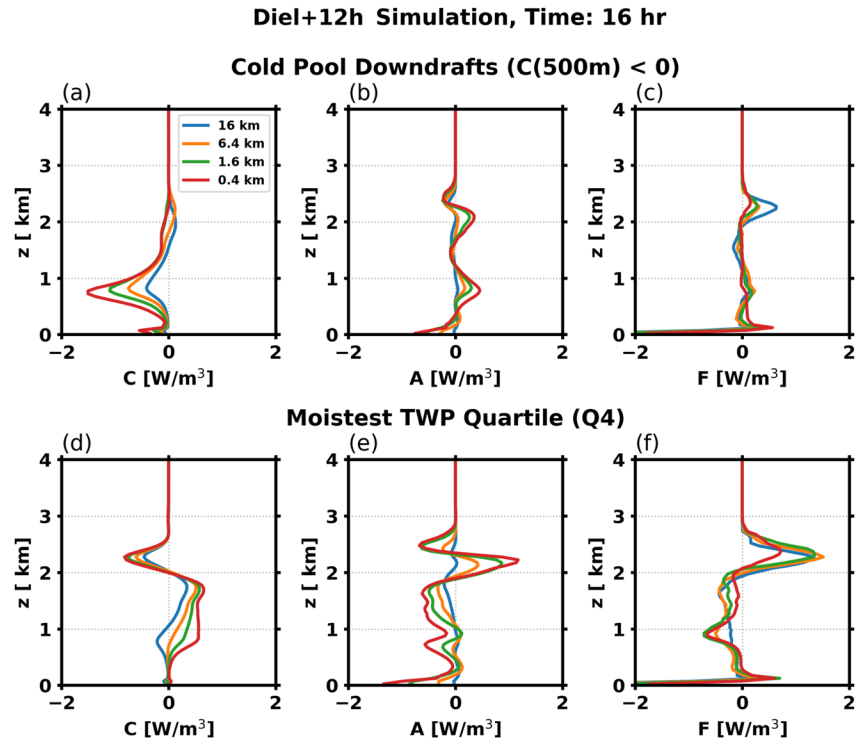
Figure B4. Profiles of the first three terms on the right hand side of Equation B1—C, $\mathcal{A}$, and $\mathcal{F}$—computed using multiple tile sizes for the Diel+12h simulation at hour 16, when the cold pools are abundant and strong. (a) The C term composited from the vertical columns in which C is negative at 500 m (i.e., where there is mesoscale divergence of total water near the surface). (b, c) The $\mathcal{A}$ and $\mathcal{F}$ terms composited from the same vertical columns as in panel (a), showing that the mesoscale divergence of total water in the mixed layer is compensated by the upward mesoscale total water advection and upward vertical total water transport by mixed layer thermal. Although both the horizontal and vertical components of the $\mathcal{A}$ and $\mathcal{F}$ terms are included, the horizontal contributions are small. (d–f) The C, $\mathcal{A}$, and $\mathcal{F}$ profiles averaged within the moistest total water path quartile or Q4 of the Diel+12h simulation.
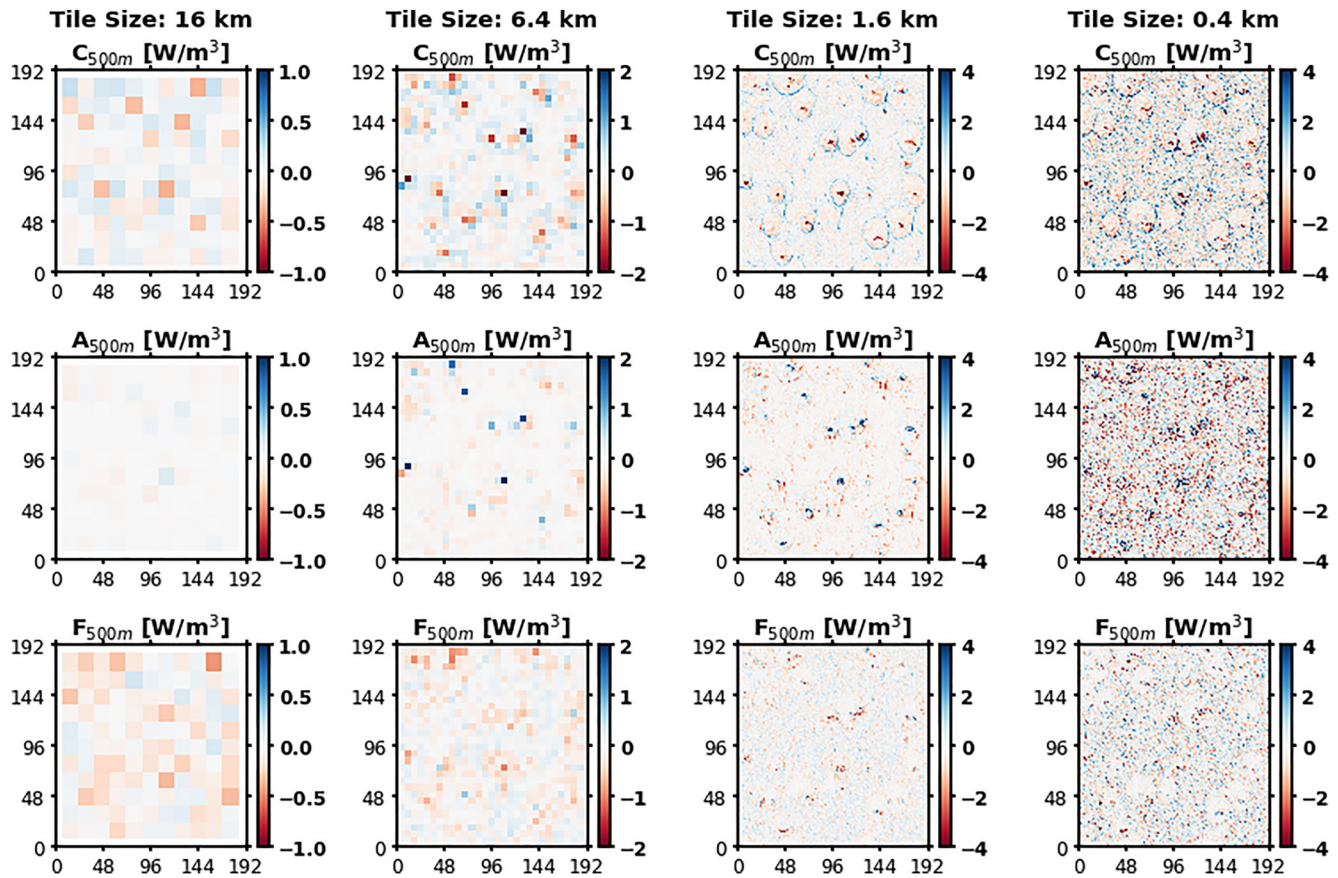
Figure B5. Snapshots of the (top) C, (middle) $\mathcal{A}$, and (bottom) $\mathcal{F}$ terms at 500 m altitude from the Diel+12h simulation at hour 16. The terms are computed at various tile sizes: 16, 6.4, 1.6, and 0.4 km. Note the different scales of the color bars for different tile sizes.

Figure B5 shows that inside the precipitating downdrafts, there is local divergence of total water ($C < 0$) in the mixed layer (approximately lower 1 km of the atmosphere), and local convergence of total water ($C > 0$) at the edges of the cold pools. These follow the signs of the surface divergence and convergence (w'' near the surface), which are the characteristics of the cold pools. The middle row shows that where $C < 0$, there is upward advection of the mesoscale total water perturbations ($\mathcal{A} > 0$). Both the horizontal and vertical contributions are shown in the snapshots, but the horizontal contributions are small. The vertical contributions of $\mathcal{A}$ are washed out when computed using larger mesoscale tile sizes. However, the surface divergence remains strong even with larger mesoscale tile sizes as long as the tile sizes are smaller than the horizontal extents of the cold pools. The cumulus-scale fluxes or $\mathcal{F}$ are smaller than the other two terms.

This is summarized by the composite profiles of C and $\mathcal{A}$ in the columns where $C < 0$ at 500 m. This represents all of the precipitating downdrafts as well as some other drier and cloud-free regions. Still, the $\mathcal{A}$ composite profiles are still positive in this level, suggesting that the total water divergence ($C < 0$) is still being compensated by the vertical advection of the total water perturbations ($\mathcal{A} > 0$). This is also in agreement with the known cloud and cold pool dynamics that as the downdrafts diverge at the surface, the gust fronts carry the extra moisture to the areas that are once cloud-free and encourage new cycle of convection through dynamical lifting of the moist air (Zuidema et al., 2012). In general, this shows that the total water convergence ($C > 0$) still takes place in the mixed layer of the moist regions, as in the Control simulation. However, with the cold pool dynamics, the total water convergence takes place over a smaller scale in the mixed layer.

Data Availability Statement

ERA5 data were generated using Copernicus Climate Change Service Information. Neither the European Commission or ECMWF is responsible for any use that may be made of the Copernicus information or data in this publication. The WACCM-CESM1 CMIP5 outputs were retrieved from the Centre for Environmental Data Analysis (CEDA) archive, and the available ensemble members were r2i1p1, r3i1p1, and r4i1p1 from the RCP 8.5 simulations. Simulation outputs from this study are available at https://csl.noaa.gov/groups/csl9/datasets/data/cloud_phys/2022-Narenpitak-etal.

References

Albrecht, B., Ghate, V., Mohrmann, J., Wood, R., Zuidema, P., Bretherton, C., et al. (2019). Cloud system evolution in the trades (CSET): Following the evolution of boundary layer cloud systems with the NSF–NCAR GV. *Bulletin of the American Meteorological Society*, *100*(1), 93–121. https://doi.org/10.1175/BAMS-D-17-0180.1

Andrews, T., Gregory, J. M., Webb, M. J., & Taylor, K. E. (2012). Forcing, feedbacks and climate sensitivity in CMIP5 coupled atmosphere-ocean climate models. *Geophysical Research Letters*, *39*(9), L09712. https://doi.org/10.1029/2012GL051607

Blossey, P. N., Bretherton, C. S., Zhang, M., Cheng, A., Endo, S., Heus, T., et al. (2013). Marine low cloud sensitivity to an idealized climate change: The CGILS LES intercomparison. *Journal of Advances in Modeling Earth Systems*, *5*(2), 234–258. https://doi.org/10.1002/jame.20025

Bony, S., & Dufresne, J. L. (2005). Marine boundary layer clouds at the heart of tropical cloud feedback uncertainties in climate models. *Geophysical Research Letters*, *32*(20), 1–4. https://doi.org/10.1029/2005GL023851

Bony, S., Lothon, M., Delanoë, J., Coutris, P., Etienne, J.-C., Aemisegger, F., et al. (2022). EUREC⁴A observations from the SAFIRE ATR42 aircraft. *Earth System Science Data Discussions*, *14*(4), 1–61. https://doi.org/10.5194/essd-2021-459

Bony, S., Schulz, H., Vial, J., & Stevens, B. (2020). Sugar, gravel, fish, and flowers: Dependence of mesoscale patterns of trade-wind clouds on environmental conditions. *Geophysical Research Letters*, *47*(7), 1–9. https://doi.org/10.1029/2019gl085988

Bony, S., Stevens, B., Ament, F., Bigorre, S., Chazette, P., Crewell, S., et al. (2017). EUREC⁴A: A field campaign to elucidate the couplings between clouds, convection and circulation. *Surveys in Geophysics*, *38*(6), 1529–1568. https://doi.org/10.1007/s10712-017-9428-0

Boucher, O., Randall, D., Artaxo, P., Bretherton, C., Feingold, G., Forster, P., et al. (2013). Clouds and aerosols. In *Climate change 2013 the physical science basis: Working group I contribution to the fifth assessment report of the intergovernmental panel on climate change*. https://doi.org/10.1017/CBO9781107415324.016

Bretherton, C. S., & Blossey, P. N. (2017). Understanding mesoscale aggregation of shallow cumulus convection using large-eddy simulation. *Journal of Advances in Modeling Earth Systems*, *9*(8), 2798–2821. https://doi.org/10.1002/2017MS000981

Bretherton, C. S., Blossey, P. N., & Jones, C. R. (2013). Mechanisms of marine low cloud sensitivity to idealized climate perturbations: A single-LES exploration extending the CGILS cases. *Journal of Advances in Modeling Earth Systems*, *5*(2), 316–337. https://doi.org/10.1002/jame.20019

Coutris, P., & Ehses, G. (2021). SAFIRE ATR42: UHSAS dataset. https://doi.org/10.25326/220

d'Almeida, G. A., Koepke, P., & Shettle, E. P. (1991). *Atmospheric aerosols: Global climatology and radiative characteristics*. A. Deepak Publication.

Feingold, G., Walko, R. L., Stevens, B., & Cotton, W. R. (1998). Simulations of marine stratocumulus using a new microphysical parameterization scheme. *Atmospheric Research*, *47*(48), 505–528. https://doi.org/10.1016/S0169-8095(98)00058-1

Gutleben, M., Groß, S., & Wirth, M. (2019). Cloud macro-physical properties in Saharan-dust-laden and dust-free North Atlantic trade wind regimes: A lidar case study. *Atmospheric Chemistry and Physics*, *19*(16), 10659–10673. https://doi.org/10.5194/acp-19-10659-2019

Gutleben, M., Groß, S., Wirth, M., Emde, C., & Mayer, B. (2019). Impacts of water vapor on saharan air layer radiative heating. *Geophysical Research Letters*, *46*(24), 14854–14862. https://doi.org/10.1029/2019GL085344

Hersbach, H., Bell, B., Berrisford, P., Hirahara, S., Horányi, A., Muñoz-Sabater, J., et al. (2020). The ERA5 global reanalysis. *Quarterly Journal of the Royal Meteorological Society*, *146*(730), 1999–2049. https://doi.org/10.1002/qj.3803

Hurrell, J. W., Holland, M. M., Gent, P. R., Ghan, S., Kay, J. E., Kushner, P. J., et al. (2013). The community Earth system model: A framework for collaborative research. *Bulletin of the American Meteorological Society*, *94*(9), 1339–1360. https://doi.org/10.1175/BAMS-D-12-00121.1

Kazil, J., Christensen, M. W., Abel, S. J., Yamaguchi, T., & Feingold, G. (2021). Realism of Lagrangian large eddy simulations driven by reanalysis meteorology: Tracking a pocket of open cells under a biomass burning aerosol layer. *Journal of Advances in Modeling Earth Systems*, *13*(12), e2021MS002664. https://doi.org/10.1029/2021MS002664

Khairoutdinov, M. F., & Randall, D. A. (2003). Cloud resolving modeling of the ARM summer 1997 IOP: Model formulation, results, uncertainties, and sensitivities. *Journal of the Atmospheric Sciences*, *60*(4), 607–625. https://doi.org/10.1175/1520-0469(2003)060⟨0607:CRMOTA⟩2.0.CO;2

Marsh, D. R., Mills, M. J., Kinnison, D. E., Lamarque, J.-F., Calvo, N., & Polvani, L. M. (2013). Climate change from 1850 to 2005 simulated in CESM1(WACCM). *Journal of Climate*, *26*(19), 7372–7391. https://doi.org/10.1175/JCLI-D-12-00558.1

Medeiros, B., Stevens, B., Held, I. M., Zhao, M., Williamson, D. L., Olson, J. G., & Bretherton, C. S. (2008). Aquaplanets, climate sensitivity, and low clouds. *Journal of Climate*, *21*(19), 4974–4991. https://doi.org/10.1175/2008JCLI1995.1

Mlawer, E. J., Taubman, S. J., Brown, P. D., Iacono, M. J., & Clough, S. A. (1997). Radiative transfer for inhomogeneous atmospheres: RRTM, a validated correlated-k model for the longwave. *Journal of Geophysical Research*, *102*(D14), 16663–16682. https://doi.org/10.1029/97JD00237

Narenpitak, P., & Bretherton, C. S. (2019). Understanding negative subtropical shallow cumulus cloud feedbacks in a near-global aquaplanet model using limited area cloud-resolving simulations. *Journal of Advances in Modeling Earth Systems*, *11*(6), 1600–1626. https://doi.org/10.1029/2018MS001572

Narenpitak, P., Kazil, J., Yamaguchi, T., Quinn, P., & Feingold, G. (2021). From sugar to flowers: A transition of shallow cumulus organization during atomic. *Journal of Advances in Modeling Earth Systems*, *13*(10), e2021MS002619. https://doi.org/10.1029/2021MS002619

Naumann, A. K., Stevens, B., Hohenegger, C., & Mellado, J. P. (2017). A conceptual model of a shallow circulation induced by prescribed low-level radiative cooling. *Journal of the Atmospheric Sciences*, *74*(10), 3129–3144. https://doi.org/10.1175/JAS-D-17-0030.1

Nuijens, L., & Siebesma, A. P. (2019). Boundary layer clouds and convection over subtropical oceans in our current and in a warmer climate. *Current Climate Change Reports*, *5*(2), 80–94. https://doi.org/10.1007/s40641-019-00126-x

Nuijens, L., & Stevens, B. (2012). The influence of wind speed on shallow marine cumulus convection. *Journal of the Atmospheric Sciences*, *69*(1), 168–184. https://doi.org/10.1175/JAS-D-11-02.1

Nuijens, L., Emanuel, K., Masunaga, H., & L'Ecuyer, T. (2017). Implications of warm rain in shallow cumulus and congestus clouds for large-scale circulations. *Surveys in Geophysics*, *38*(6), 1257–1282. https://doi.org/10.1007/s10712-017-9429-z

Nuijens, L., Stevens, B., & Siebesma, A. P. (2009). The environment of precipitating shallow cumulus convection. *Journal of the Atmospheric Sciences*, *66*(7), 1962–1979. https://doi.org/10.1175/2008JAS2841.1

Pincus, R., Fairall, C. W., Bailey, A., Chen, H., Chuang, P. Y., de Boer, G., et al. (2021). Observations from the NOAA P-3 aircraft during ATOMIC. *Earth System Science Data Discussions*, 1–25. https://doi.org/10.5194/essd-2021-11

Quinn, P. K., Thompson, E., Coffman, D. J., Baidar, S., Bariteau, L., Bates, T. S., et al. (2021). Measurements from the *RV Ronald H. Brown* and related platforms as part of the Atlantic Tradewind Ocean-Atmosphere Mesoscale Interaction Campaign (ATOMIC). *Earth System Science Data Discussions*, *13*(4), 1–41. https://doi.org/10.5194/essd-2020-331

Rasp, S., Schulz, H., Bony, S., & Stevens, B. (2020). Combining crowd-sourcing and deep learning to explore the meso-scale organization of shallow convection. *Bulletin of the American Meteorological Society*, *101*(11), E1980–E1995. https://doi.org/10.1175/BAMS-D-19-0324.1

Rauber, R. M., Stevens, B., Ochs, H. T., Knight, C., Albrecht, B. A., Blyth, A. M., et al. (2007). Rain in shallow cumulus over the ocean: The RICO campaign. *Bulletin of the American Meteorological Society*, *88*(12), 1912–1928. https://doi.org/10.1175/BAMS-88-12-1912

Rieck, M., Nuijens, L., & Stevens, B. (2012). Marine boundary layer cloud feedbacks in a constant relative humidity atmosphere. *Journal of the Atmospheric Sciences*, *69*(8), 2538–2550. https://doi.org/10.1175/JAS-D-11-0203.1

Rolph, G., Stein, A., & Stunder, B. (2017). Real-time environmental applications and display system: Ready. *Environmental Modelling & Software*, *95*, 210–228. https://doi.org/10.1016/j.envsoft.2017.06.025

Schulz, H. (2021). C^{3}ONTEXT: A common consensus on convective organization during the EUREC^{4}A eXperiment. *Earth System Science Data Discussions*, *2021*(3), 1–27. https://doi.org/10.5194/essd-2021-427

Schulz, H., Eastman, R., & Stevens, B. (2021). Characterization and evolution of organized shallow convection in the downstream north Atlantic trades. *Journal of Geophysical Research: Atmospheres*, *126*(17), e2021JD034575. https://doi.org/10.1029/2021JD034575

Seifert, A., & Heus, T. (2013). Large-eddy simulation of organized precipitating trade wind cumulus clouds. *Atmospheric Chemistry and Physics*, *13*(11), 5631–5645. https://doi.org/10.5194/acp-13-5631-2013

Stein, A. F., Draxler, R. R., Rolph, G. D., Stunder, B. J. B., Cohen, M. D., & Ngan, F. (2015). NOAA's HYSPLIT atmospheric transport and dispersion modeling system. *Bulletin of the American Meteorological Society*, *96*(12), 2059–2077. https://doi.org/10.1175/BAMS-D-14-00110.1

Stephan, C. C., Schnitt, S., Schulz, H., Bellenger, H., de Szoeke, S. P., Acquistapace, C., et al. (2021). Ship- and island-based atmospheric soundings from the 2020 EUREC^{4}A field campaign. *Earth System Science Data*, *13*(2), 491–514. https://doi.org/10.5194/essd-13-491-2021

Stevens, B., Ackerman, A. S., Albrecht, B. A., Brown, A. R., Chlond, A., Cuxart, J., et al. (2001). Simulations of trade wind cumuli under a strong inversion. *Journal of the Atmospheric Sciences*, *58*(14), 1870–1891. https://doi.org/10.1175/1520-0469(2001)058⟨1870:SOTWCU⟩2.0.CO;2

Stevens, B., Bony, S., Brogniez, H., Hentgen, L., Hohenegger, C., Kiemle, C., et al. (2020). Sugar, gravel, fish and flowers: Mesoscale cloud patterns in the trade winds. *Quarterly Journal of the Royal Meteorological Society*, *146*(726), 141–152. https://doi.org/10.1002/qj.3662

Stevens, B., Bony, S., Farrell, D., Ament, F., Blyth, A., Fairall, C., et al. (2021). EUREC^{4}A. *Earth System Science Data Discussions*, 1–78. https://doi.org/10.5194/essd-2021-18

Tompkins, A. M., & Semie, A. G. (2017). Organization of tropical convection in low vertical wind shears: Role of updraft entrainment. *Journal of Advances in Modeling Earth Systems*, *9*(2), 1046–1068. https://doi.org/10.1002/2016MS000802

Touzé-Peiffer, L., Vogel, R., & Rochetin, N. (2022). Cold pools observed during EUREC4A: Detection and characterization from atmospheric soundings. *Journal of Applied Meteorology and Climatology*, *61*(5), 593–610. https://doi.org/10.1175/JAMC-D-21-0048.1

vanZanten, M. C., Stevens, B., Nuijens, L., Siebesma, A. P., Ackerman, A. S., Burnet, F., et al. (2011). Controls on precipitation and cloudiness in simulations of trade-wind cumulus as observed during RICO. *Journal of Advances in Modeling Earth Systems*, *3*(2), M06001. https://doi.org/10.1029/2011MS000056

Vial, J., Vogel, R., & Schulz, H. (2021). On the daily cycle of mesoscale cloud organization in the winter trades. *Quarterly Journal of the Royal Meteorological Society*, *147*(738), 2850–2873. https://doi.org/10.1002/qj.4103

Vial, J., Vogel, R., Bony, S., Stevens, B., Winker, D. M., Cai, X., et al. (2019). A new look at the daily cycle of trade wind cumuli. *Journal of Advances in Modeling Earth Systems*, *11*(10), 3148–3166. https://doi.org/10.1029/2019MS001746

Vogel, R., Konow, H., Schulz, H., & Zuidema, P. (2021). A climatology of trade-wind cumulus cold pools and their link to mesoscale cloud organization. *Atmospheric Chemistry and Physics*, *21*(21), 16609–16630. https://doi.org/10.5194/acp-21-16609-2021

Xu, K.-M., Cheng, A., & Zhang, M. (2010). Cloud-resolving simulation of low-cloud feedback to an increase in sea surface temperature. *Journal of the Atmospheric Sciences*, *67*(3), 730–748. https://doi.org/10.1175/2009JAS3239.1

Yamaguchi, T., Feingold, G., Kazil, J., & McComiskey, A. (2015). Stratocumulus to cumulus transition in the presence of elevated smoke layers. *Geophysical Research Letters*, *42*(10), 10478–10485. https://doi.org/10.1002/2015GL066544

Zelinka, M. D., Myers, T. A., McCoy, D. T., Po-Chedley, S., Caldwell, P. M., Ceppi, P., et al. (2020). Causes of higher climate sensitivity in CMIP6 models. *Geophysical Research Letters*, *47*(1), e2019GL085782. https://doi.org/10.1029/2019GL085782

Zelinka, M. D., Zhou, C., & Klein, S. A. (2016). Insights from a refined decomposition of cloud feedbacks. *Geophysical Research Letters*, *43*(17), 9259–9269. https://doi.org/10.1002/2016GL069917

Zhang, M., Bretherton, C. S., Blossey, P. N., Austin, P. H., Bacmeister, J. T., Bony, S., et al. (2013). CGILS: Results from the first phase of an international project to understand the physical mechanisms of low cloud feedbacks in single column models. *Journal of Advances in Modeling Earth Systems*, *5*(4), 826–842. https://doi.org/10.1002/2013MS000246

Zuidema, P., Li, Z., Hill, R. J., Bariteau, L., Rilling, B., Fairall, C., et al. (2012). On trade wind cumulus cold pools. *Journal of the Atmospheric Sciences*, *69*(1), 258–280. https://doi.org/10.1175/JAS-D-11-0143.1

Zuidema, P., Sedlacek, A. J., III., Flynn, C., Springston, S., Delgadillo, R., Zhang, J., et al. (2018). The Ascension Island boundary layer in the remote Southeast Atlantic is often smoky. *Geophysical Research Letters*, *45*(9), 4456–4465. https://doi.org/10.1002/2017GL076926

Zuidema, P., Torri, G., Muller, C., & Chandra, A. (2017). A survey of precipitation-induced atmospheric cold pools over oceans and their interactions with the larger-scale environment. *Surveys in Geophysics*, *38*(6), 1283–1305. https://doi.org/10.1007/s10712-017-9447-x